STUDY OF LIQUID METALS

BY ELECTROSTATIC LEVITATION

Thesis by
John Jian-Zhong Li

In Partial Fulfillment of the Requirements
for the Degree of
Doctor of Philosophy

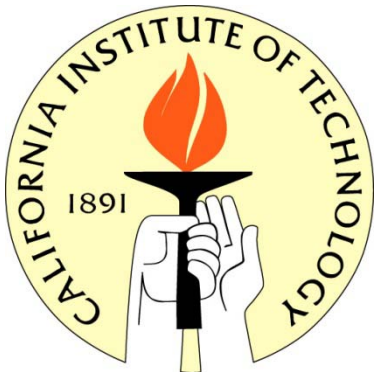

California Institute of Technology
Pasadena, California
2009
(Defended [June, 1, 2009])

To my parents, my wife and my son

Acknowledgments

Studying at Caltech marks the most important period of my life so far. I still remember how I felt when I first came to Caltech from Missouri during a Christmas. It amazed me to see so many flowers in winter on campus. So many years have passed and I feel so grateful to the many people who have given me helping hands.

First of all, I would like to thank my advisor, Professor Bill Johnson, not only for providing me an opportunity to study at Caltech; he has given me much creative advice throughout my academic research. His guidance in leading my life, his encouragement and compassion helped me to stand up and to overcome the challenges due to my physical condition that I suffered through for years. I will always treasure my experience of studying under his guidance.

Secondly, I would like to thank to my co-advisor, Dr. Won-Kyu Rhim. The electrostatic levitator (ESL) invented by Won-Kyu offered me an opportunity to investigate the metals in the undercooled liquid state. The experience of setting up the ESL changed me from a theoretician to an experimentalist. The encouragement he gave to me when I worked on repairing expensive equipment let me gain both experience and confidence in laboratory work. The spiritual guidance by Won-Kyu helped me learn how to be a good person. I will always remember that we were both singing in the lab after work. He is a good singer.

I also thank Professor Konrad Samwer of Georg-August-Universität, Professor Hans Fetcht of University of Ulm, Professor Jan Schroers of Yale University, and Professor

Sven Bossuyt of Vrije University Brussels. All of them have given me many ideas on my research. I am grateful to Paul Kim, Donghua Xu, Gang Duan, Aaron Wiest, Jin-Yoo Suh, G.Z. Fan, and S.M. Chathoth for providing me samples, Marios Demetriou for helping me with the theoretical background of crystallization. The friendship from my group members Sundeep Muhkerjee, Zhenhua Zhou, Mary-Laura Lind, Joe Schramm, Glenn Garrett, Douglas Hofmann, John Harmon, Dale Connerand and Mo Li has made my life at Caltech more colorful. My thanks also go to Pam Albertson, who has given me much administrative assistance.

I would like to thank to my former advisors Professor William Yelon at University of Missouri-Columbia, and Dr. Y. F. Cheng at Atomic Energy Institute of China in Beijing, who provided me an opportunity to study in the US.

My ex-wife, Haiyan Gao, has given me courage to finish my Ph.D. and my lovely son, Calvin, always reminds me of my unfulfilled dream. My parents, my brother and sisters have supported me to overcome the difficulties I have experienced.

I would like to thank to my beautiful wife Vivian for her love, care, and understanding.

Finally, I would like to thank to Master Li Hongzhi for teaching me Falun Dafa and its principle, “Truthfulness, Compassion and Forbearance”, from which I have obtained a better understanding of my life, and improved my health.

Abstract

With the development of bulk metallic glasses (BMG) in recent years, more and more scientists in solid state physics are trying to understand the mechanism of glass-formation in terms of thermodynamics and kinetics, while engineers in metallurgy are trying different compositions and processes to improve the mechanical properties of BMGs and their composites.

Glasses are nothing but frozen liquids. So far most of the studies of metallic glasses have been below the glass transition temperature because molten metallic liquids are chemically reactive with the container walls. For this reason, we used the Electrostatic Levitation (ESL) method that was developed by Dr. Won-Kyu Rhim.

In this thesis, the instrumentation of the ESL is described. Discussion on the advantages and disadvantages of ESL is given by comparing with the other levitation methods. Because of the advantage in sample position stability over all the other levitation methods, the ESL facility at Caltech is uniquely capable of measuring the viscosity and thermophysical properties of liquid metals in the undercooled temperature range. The ESL was further improved at Caltech to reduce temperature gradients on a sample and increase the stability of the sample positioning with a tetrahedral laser heating system.

Using such an improved ESL, thermophysical properties of some evaporative metallic liquids such as Ti and silicon-germanium alloys have been successfully studied and mass loss as well as composition changes could be accounted for.

Several BMGs developed at Johnson group at Caltech have been studied using ESL. Among the liquid thermodynamics and kinetic properties of interest, special attention has been paid on to measurements of the TTT curve, viscosity, and volume changes with temperature. These data give useful insight on the glass-forming mechanism. Through these studies, guidelines in the search for good ductile metallic glass-formers have emerged. Discussing these guidelines is an important part of this thesis.

Finally, we discuss an investigation to understand observed hysteresis in the viscosity and the so-called threshold temperature that has been observed in some of the best glass-forming metallic liquids. We conclude this investigation with a hypothesis of a liquid-to-liquid phase transition that occurs above liquidus temperatures in several systems that we have studied.

Table of Contents

List of Figures

Chapter1

Chapter 2

Chapter 3

Chapter 4

Chapter 5

Chapter 6

List of Tables

1 Introduction

1.1 Thermophysical Properties of Liquid Metals

Thermophysical properties of metals in molten state have not been studied as much as in the solid state because of the experimental difficulties caused by:

- High temperature
- Chemical reactivity (no crucible materials)
- Crystallization triggered by the container walls for liquids in the undercooled temperature range.

Containerless methods have been developed to study the properties of liquid metals. The electromagnetic levitator (EML) [1] has been commonly used to levitate and melt metallic samples. Since the levitation and heating cannot be decoupled in an EML, flowing gases have been used to cool levitated liquid metals during levitation. This limits the cleanliness of the sample surfaces and creates instabilities in the sample's position and irregularity in its shape. Microgravity has been proposed as an approach to alleviate these problems: a) Parabolic flights and drop tubes have been used to achieve a microgravity environment for timer of about 4 to 20 seconds [2, 3], which is not long enough for most of studies on liquid metals; b) A space shuttle provides an ideal environment of microgravity for studying liquid metals [4] but the cost of launching a payload into earth orbit is high and the waiting period is long. The first Electrostatic Levitator (ESL) was developed by Won-Kyu Rhim, and has allowed unique studies of liquid metals [5--14]. After being upgraded both in software control and the hardware

setup, the ESL at Caltech has enabled us to challenge the limits of measurements on metals in liquid state at elevated temperature.

1.2 Studying Liquids to Improve the Quality of Solids

Studying the properties of liquid provides some unique information that can improve the processing and qualities of materials in the solid state. With the recent development of BMGs and their composites, a better understanding of the thermophysical properties of these alloys in liquid state has become very important in developing new BMG alloys and characterizing the glassy solids [15--17]. With the easy control of sample temperature and removal of the disturbing influence from container walls, the ESL, along with its various non-contact diagnostic techniques, can provide a variety of data on the thermophysical properties of these metallic alloys in liquid state.

1.2.1 Heating history and thermophysical properties

Most glassy alloys are made by cooling from their molten state. The thermal history of the process influences the structure and properties of the materials. Among these, is the influence of the so-called threshold temperature. This is defined by the difference between the liquidus temperature and the temperature required to preheat the sample to obtain good glass-forming ability. Figure 1.1 shows an example of the threshold temperature influence on the degree of liquid undercooling which can be achieved [18].

The cooling curve of a sample provides information on the phase transition to the crystalline state as illustrated in Figure 1.2. During the cooling of $Zr_{57}Cu_{15.4}Ni_{12.6}Al_{10}Nb_5$ (Vit106), a 12KV AC pulse was applied on the z-direction electrodes, and was observed to trigger a crystallization of the liquid.

When a triggering pulse was applied at a given undercooled temperature, crystal nucleation was observed in the liquid and the crystallization progressed as the sample was cooled. We see in Figure 1.1 that the incubation period prior to the rapid crystallization varies as a function of the initial starting temperature.

Depending on the temperature when the triggering was applied, the liquid went through an undercooling below its melting temperature, followed by a recalescence back to a higher temperature. The Vit106 sample vitrifies in the absence of the triggering when allowed to cool to low temperature.

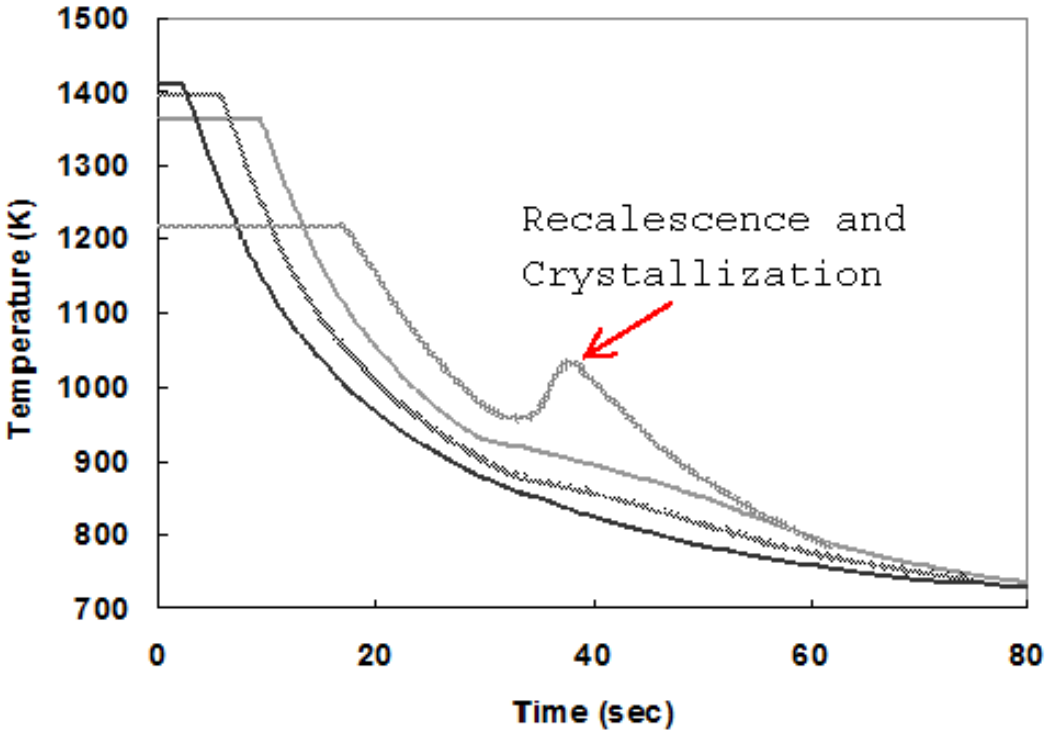

Figure 1.1: The cooling curves obtained for $Zr_{57}Cu_{15.4}Ni_{12.6}Al_{10}Nb_5$ (Vit106) with different levels of overheating [9]

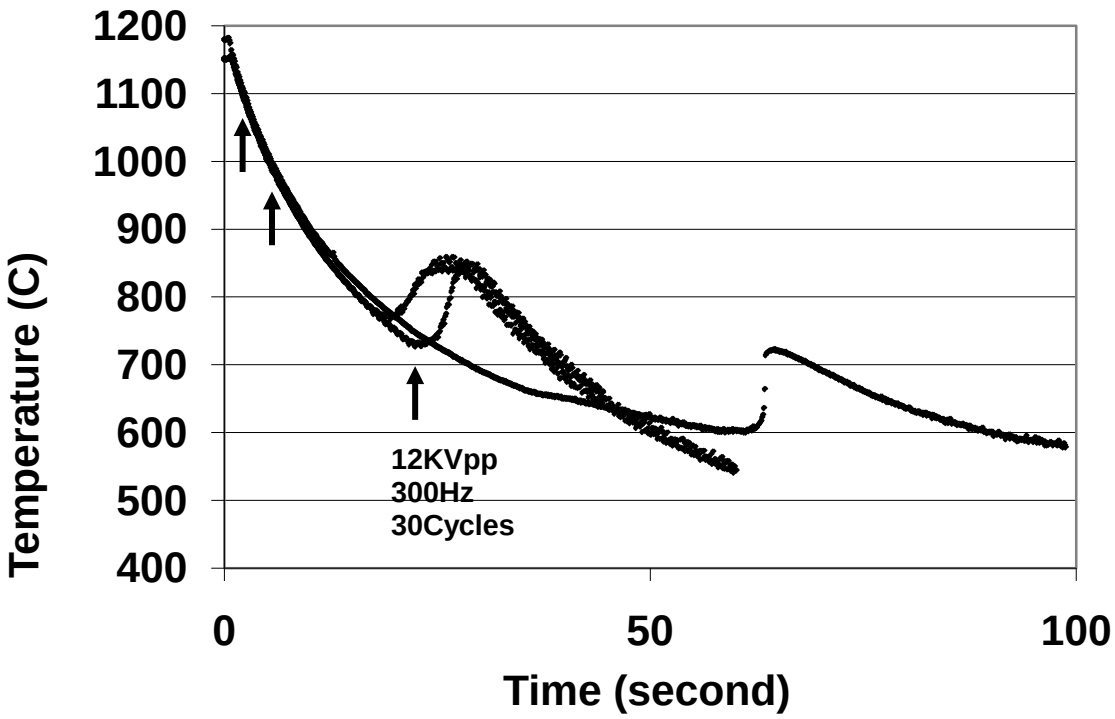

Figure 1.2: Cooling curve of $Zr_{57}Cu_{15.4}Ni_{12.6}Al_{10}Nb_5$ (Vit106) when crystallization was triggered at different temperatures by applying a 12KV AC pulse

1.2.2 Thermodynamic properties of undercooled liquids

Thermophysical properties of liquid metals are very important, but often hard to obtain. The specific volume and thermal expansion coefficient of liquid are important, for example, in precision mold casting. The liquid surface tension is important for modeling the flow of liquids at high viscosity. According to the free volume model [19], the viscosity of a liquid is related to the "free volume" of the liquid, so the changes of liquid volume determine the changes of viscosity.

$$\eta = \eta_0 \, \boldsymbol{Exp} \left(\frac{\boldsymbol{bv_0}}{\boldsymbol{v_f}}\right), \tag{1.1}$$

where v_f denotes the average free volume per atom, and bv_0 the critical volume for flow. Liquid volume changes with temperature can also reveal the structural changes in liquid [20]. Equation 1.1 links the thermodynamic and kinetic properties of the liquid.

1.2.3 The driving force for phase transition to crystalline state

At melting temperature, the Gibbs free energy of the liquid equals the solid. The difference in enthalpy between crystalline and liquid at the melting temperature is the heat of fusion. This determines the amount of heat released from the liquid-solid phase transition. By measuring the specific heat of an undercooled liquid and comparing it with the solid, we can determine the difference of Gibbs free energy between liquid and crystalline as a function of temperature. This difference is the driving force of the phase transition. This is not only important in modeling the phase transition but also important in industrial processing of molten alloys.

1.2.4 Kinetic properties of liquid metals

The change of viscosity with the temperature is important in understanding the kinetic aspect of a metallic liquid. The temperature dependence of the liquid viscosity can be characterized by the fragility index which is defined as [21]

$$m = \frac{d(log(\eta))}{d(\frac{T_g}{T})}\Big|_{T=T_g}. \quad (1.2)$$

Several models have been used to fit the experimental viscosity data [22--24]. The measurements of viscosity on liquid metals can provide insight into structural changes in the liquid during cooling and freezing to the glassy state.

1.3 Motivation and Objectives

The main objective of this thesis is to investigate the thermophysical properties of several different alloys in liquid state, and to understand the role of thermodynamic and kinetic properties of a liquid in its crystallization. The instrumentation upgrades on the ESL at Caltech using a tetrahedral laser heating system have enabled us to measure certain thermophysical properties of various alloys in their liquid state for the first time [25, 26].

1.3.1 Thermophysical properties of the Liquid Ti-6Al-4V alloy

The commercial alloy Ti-6Al-4V has been widely used in many industries, but several of its thermophysical properties in its liquid state were unknown when this work began. This lack of property of data on the molten alloy has limited the ability to understand and model the processing of the material from the melts by casting and other forms of solidification.

Thermophysical property measurements on Ti-6Al-4V not only provide some important data for industry but also demonstrated the capability of the upgraded ESL system. The complete set of thermophysical properties measured by ESL helps our understanding of this commercially important alloy.

1.3.2 Investigating molten Si, Ge and Si_xGe_{1-x}

Si and Ge are typical semiconductors and they undergo a semiconductor to metal transition on melting. However, only a few measurements of their thermophysical properties in the liquid state have been carried out. This has limited our knowledge of their liquid properties.

Ge–Si alloys have been used in optics for high-brilliance X-ray sources such as synchrotron radiation, as well in more electronic devices. Ge-Si alloys form random diamond cubic solid solutions over the entire concentration range. Their local structure in liquid state has been studied by neutron diffraction, X-ray diffraction and EXAFS. Using the ESL facility at Caltech, we studied the thermophysical properties of the liquids to achieve a better understanding of structural changes and alloying effects in the melts.

1.3.3 Studies of bulk metallic glass alloys in their molten states

With the development of BMG's in recent years, the requirement of low cooling rates alloys with high ductility became important for their structural applications. Study of BMGs in the liquid state helps to understand the mechanism of glass-formation in BMGs [18, 27--31]. By comparing changes of thermophysical properties with the systematical composition changes from binary to multi-component alloys, a better understanding of

the liquid to crystal phase transition and structural changes in the liquid has made possible developing new materials with enhanced glass-forming ability and assisted in process design for industrial applications of BMGs [15].

Special attention has been paid to measurements of specific volume changes with the temperature, the Time-Temperature-Transformation (T-T-T) curves for crystallization, and viscosity changes with temperature. These provide information useful in processing as well as hard-to-find data such as interfacial tension between solid and liquid.

1.4 Thesis Overview and Key Contributions

The ESL technique and instrumentation of ESL is introduced in Chapter 2. The advantages of the novel tetrahedral laser heating system over the previous one-beam heating system are discussed. The tetrahedral heating system used at Caltech is the only one of its kind in the world. This provides a stable sample levitation and uniform sample temperature.

In Chapter 3, various non-contact methods for measuring thermophysical properties of levitated molten metallic samples in the ESL are described.

Results of measurements on the commercial alloy Ti-6Al-4Vare reported in Chapter 4, with a complete analysis of thermodynamic properties measured in its molten state. For the first time, we have achieved stable levitation of this sample and successfully measured its thermophysical properties in undercooled temperature range.

In Chapter 5, a new challenge on ESL is reported. Measurements on the thermophysical properties of liquid Si_xGe_{1-x}, where x= 0, 0.25, 0.5, 0.75 and 1 have been carried out. The

challenge is not only by the difficulties of measuring a chemically reactive molten semiconductor, but also the evaporation of Ge from molten Si_xGe_{1-x} samples which caused changes in mass and composition during the measurements. This made it more difficult to obtain accurate information on the specific volume and the density. Many results described in this thesis are the first data reported for the thermophysical properties of these alloys in the liquid state. These results provide new insights which will be valuable for future theoretical modeling and for processing these materials in the molten state.

Chapter 6 reports thermophysical properties of several BMGs measured by ESL. This study is focused on the thermodynamics and kinetic properties, the glass-forming ability (GFA) and the properties of BMGs in the glassy state. The results of this study provide guidelines for finding good glass-forming metallic liquids and glasses with good ductility.

The investigation on the volume changes in liquid Vit1 ($Zr_{41.2}Ti_{13.8}Ni_{10}Cu_{12.5}Be_{22.5}$) and LM7 alloys suggests a liquid-to-liquid phase transition. This explains the reported hysteresis in viscosities of liquid Vit1 [32] and liquid LM7 above liquidus temperatures. This transition also appears to be related to the reported threshold temperature effect [30].

1.5 References

[1] K. Eckler, R. F. Cochrane, D. M. Herlach, B. Feuerbacher, and M. Jurisch, Physical Review B **45**, 5019 (1992).

[2] S. M. Chathoth, B. Damaschke, K. Samwer, and S. Schneider, Applied Physics. Letter. **93**, 3 (2008).

[3] P. von Kampen, U. Kaczmarczik, and H. J. Rath, (Pergamon-Elsevier Science Ltd, 2006), p. 278.

[4] R. K. Wunderlich, R. A. Sagel, C. Ettel, H. J. Fecht, D. S. Lee, S. Glade, and W. L. Johnson, edited by W. H. Hofmeister, J. R. Rogers, N. B. Singh, S. P. Marsh and P. W. Vorhees (TMS-Miner. Metals & Mater. Soc, Rosemont, IL, & San Diego, CA,, 1999), p. 53.

[5] W. K. Rhim, S. K. Chung, D. Barber, K. F. Man, G. Gutt, A. Rulison, and R. E. Spjut, Review of Scientific Instruments **64**, 2961 (1993).

[6] W. K. Rhim, Microgravity Science and Technology **8**, 46 (1995).

[7] W. K. Rhim, S. K. Chung, A. J. Rulison, and R. E. Spjut, (Plenum Publ Corp,1997), p. 459.

[8] W. K. Rhim and T. Ishikawa, Review of Scientific Instruments **69**, 3628 (1998).

[9] W. K. Rhim and T. Ishikawa, (Kluwer Academic/Plenum Publ, 2000), p. 429.

[10] W. K. Rhim and T. Ishikawa, Review of Scientific Instruments **72**, 3572 (2001).

[11] W. K. Rhim and K. Ohsaka, Journal of Crystal Growth **208**, 313 (2000).

[12] W. K. Rhim, K. Ohsaka, P. F. Paradis, and R. E. Spjut, Review of Scientific Instruments **70**, 2796 (1999).

[13] W. K. Rhim and P. F. Paradis, Review of Scientific Instruments **70**, 4652 (1999).

[14] A. J. Rulison and W. K. Rhim, Review of Scientific Instruments **65**, 695 (1994).

[15] W. L. Johnson, MRS Bull. **24**, 42 (1999).

[16] D. C. Hofmann, J. Y. Suh, A. Wiest, M. L. Lind, M. D. Demetriou, and W. L. Johnson, Proceedings of the National Academy of Sciences of the United States of America **105**, 20136 (2008).

[17] A. Wiest, J. S. Harmon, M. D. Demetriou, R. D. Conner, and W. L. Johnson, Scripta Materialia **60**, 160 (2009).

[18] S. Mukherjee, Z. Zhou, J. Schroers, W. Johnson, and W. Rhim, Applied Physics. Letter **84**, 5010 (2004).

[19] M. H. Cohen and G. S. Grest, Physical Review B **20**, 1077 (1979).

[20] J. J.Z. Li, W. Johnson, and W. Rhim, Applied Physics Letter **89** (2006).

[21] R. Bohmer, K. L. Ngai, C. A. Angell, and D. J. Plazek, J. Chem. Phys. **99**, 4201 (1993).

[22] G. J. Fan, M. Freels, H. Choo, P. K. Liaw, J. J.Z. Li, W. K. Rhim, W. L. Johnson, P. Yu, and W. H. Wang, Applied Physics Letter **89**, 3 (2006).

[23] J. S. Harmon, M. D. Demetriou, and W. L. Johnson, Applied Physics Letter **90** (2007).

[24] W. L. Johnson, M. D. Demetriou, J. S. Harmon, M. L. Lind, and K. Samwer, MRS Bull. **32**, 644 (2007).

[25] S. Bossuyt, J. Schroers, W. Rhim, and W. Johnson, Review of Scientific Instruments **76** (2005).

[26] J. Schroers, S. Bossuyt, W. Rhim, J. J.Z. Li, Z. Zhou, and W. Johnson, Review of Scientific Instruments **75**, 4523 (2004).

[27] Y. Kim, R. Busch, W. Johnson, A. Rulison, And W. Rhim, Applied Physics Letter **65**, 2136 (1994).

[28] S. Mukherjee, H. Kang, W. Johnson, and W. Rhim, Physical Review B **70** (2004).

[29] S. Mukherjee, J. Schroers, W. Johnson, and W. Rhim, Physical Review Letters **94** (2005).

[30] S. Mukherjee, J. Schroers, Z. Zhou, W. Johnson, And W. Rhim, Acta Materialia **52**, 3689 (2004).

[31] S. Mukherjee, Z. Zhou, W. Johnson, And W. Rhim, Journal Of Non-Crystalline Solids **337**, 21 (2004).

[32] C. Way, P. Wadhwa, And R. Busch, Acta Materialia **55**, 2977 (2007).

2 Instrumentation on the Electrostatic Levitator

2.1 Introduction

The electrostatic levitator (ESL) at Caltech, which was upgraded from the original ESL developed by Rhim *et al.* [1], is extensively used in our experiments as a non-contact containerless material processing facility. Containerless methods have been used to investigate the thermophysical properties of materials in liquid state, especially in undercooled temperature range, to avoid the chemical reaction of the liquid with container walls and related heterogeneous nucleation. Compared with other containerless methods, we find that the ESL has many advantages over the others. EML (electromagnetic levitation), can easyly levitate conducting materials [2], while aerodynamic levitation can also levitate non-conducting materials [3], but both methods cause distortion in sample shape from spherical, which prevents accurate measurements of many properties such as volume, viscosity and surface tension. These two methods also need cooling gases and the impurities in the gases contaminate the surface of the samples. This contamination not only reduces the degree of undercooling, but also changes the surface properties such as emissivity. The vacuum chamber of ESL at Caltech has a base pressure of 10^{-8} torr, which is so far one of the cleanest facilities used in levitating molten metal. Good stability of the levitated sample is another advantage for ESL in measuring viscosity and other properties of liquid metals. Parabolic flights and drop towers offer only 5 to 20 seconds of reduced gravity for measurements, so the stability of the sample is hard to achieve [4, 5]. To measure the viscosity and surface tension of a molten metal, an oscillation is generated along the z-direction while the

oscillation amplitude and frequency is recorded. This requires a stable levitation of the sample and a rotation only along the z-direction. The upgraded ESL with its tetrahedral heating system was developed to further increase the stability of the sample and to reduce the temperature gradients on the samples.

2.2 Levitation and Position Control

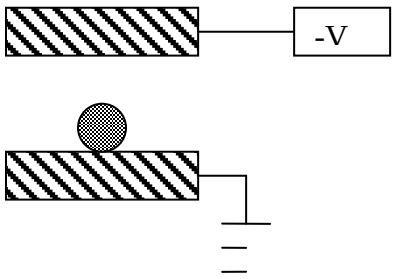

Fig.2.1: Schematic Diagram of one-dimensional ESL

The basic function of an ESL is to levitate a sample against the gravitational force by applying an appropriately controlled electric field to a charged sample so that the sample can be kept at a predetermined position in a vacuum chamber. Once the sample is prepared in a levitated state it is subjected to various thermal cycles or it can be interrogated for its properties using various non-contact diagnostic techniques. Figure 2.1 is a schematic diagram of a one-dimensional ESL with controls in the vertical direction to balance the gravity force. In a similar way the sample position can be controlled in all three dimensions in a real ESL system, as illustrated in Figure 2.2.

2.2.1 Charging the sample

In Figure 2.1, when a negative voltage is applied to the top electrode a net positive charge on the surface of a grounded sample will be created by the applied electric field. This

induced charge on the sample increases with the increase in voltage until enough sample charge is accumulated for levitation. To keep a consistent polarity with that induced by the other charging methods, positive charging is chosen as the initial charge [6]. When the sample is levitated, the levitation force provided by the static electric field balances the gravity force satisfying the following force balance equation:

$$Mg = Q * E = Q * \left(\frac{V}{d}\right) \tag{2.1}$$

where *m* is the sample mass, *Q* the sample charge, *V* the voltage applied, and *d* the distance between the top and the bottom electrode. From Equation 2.1 the sample charge *Q* is determined by *mgd/V*.

The 3-D position of the sample is detected using two sets of two-dimensional position detectors, and the stable sample positioning is achieved by 3-D PID (Position Integral Derivative) feedback control. The three feedback signals are applied to x and y control electrodes in addition to the top “z” electrode. A three-dimensional ESL is illustrated in Figure 2.2. The control loop operates at 1000Hz.

When a levitated sample is heated by laser beams, the initial charges on the sample tend to be partially lost. The sample becomes fully charged as the thermionic temperature (which is about 1300K) is reached and the thermionic emission of electrons reaches a steady state. To keep the sample positively charged at the temperature below the thermionic temperature, another charging method, UV radiation by a focused xenon lamp, is applied to charge the sample by photoemission.

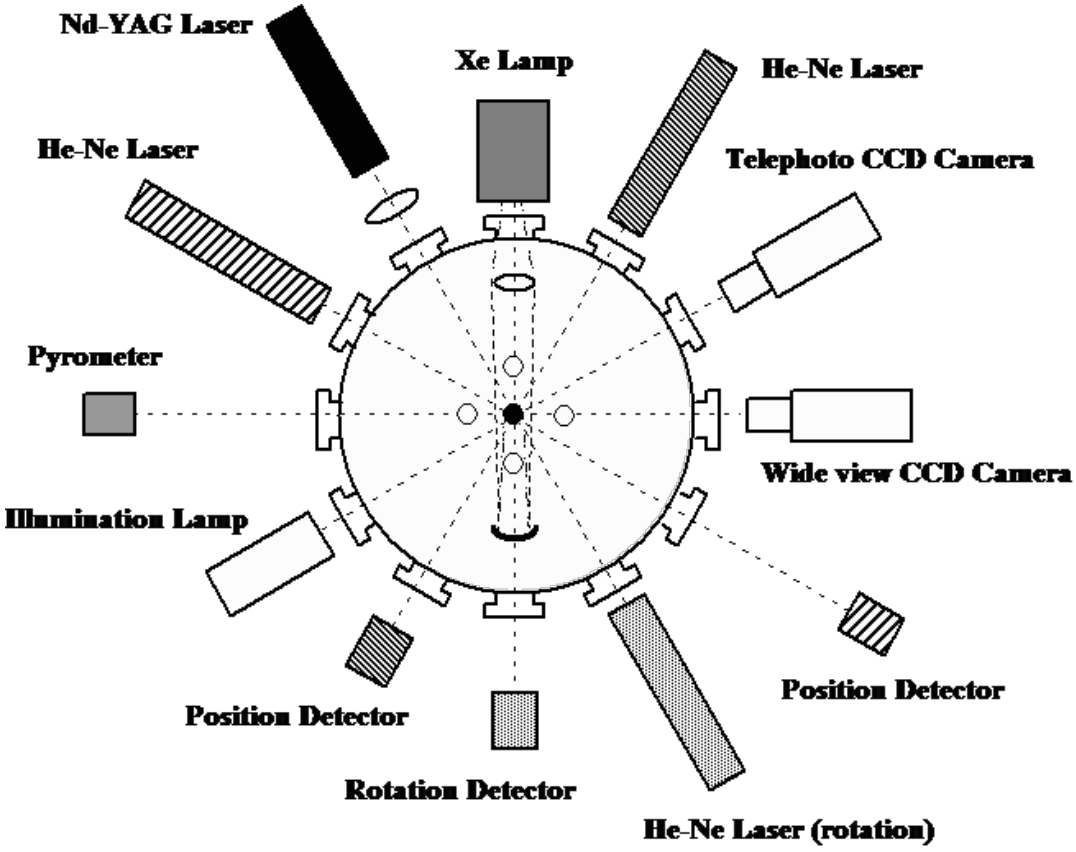

Figure 2.2: Schematic illustration of an ESL

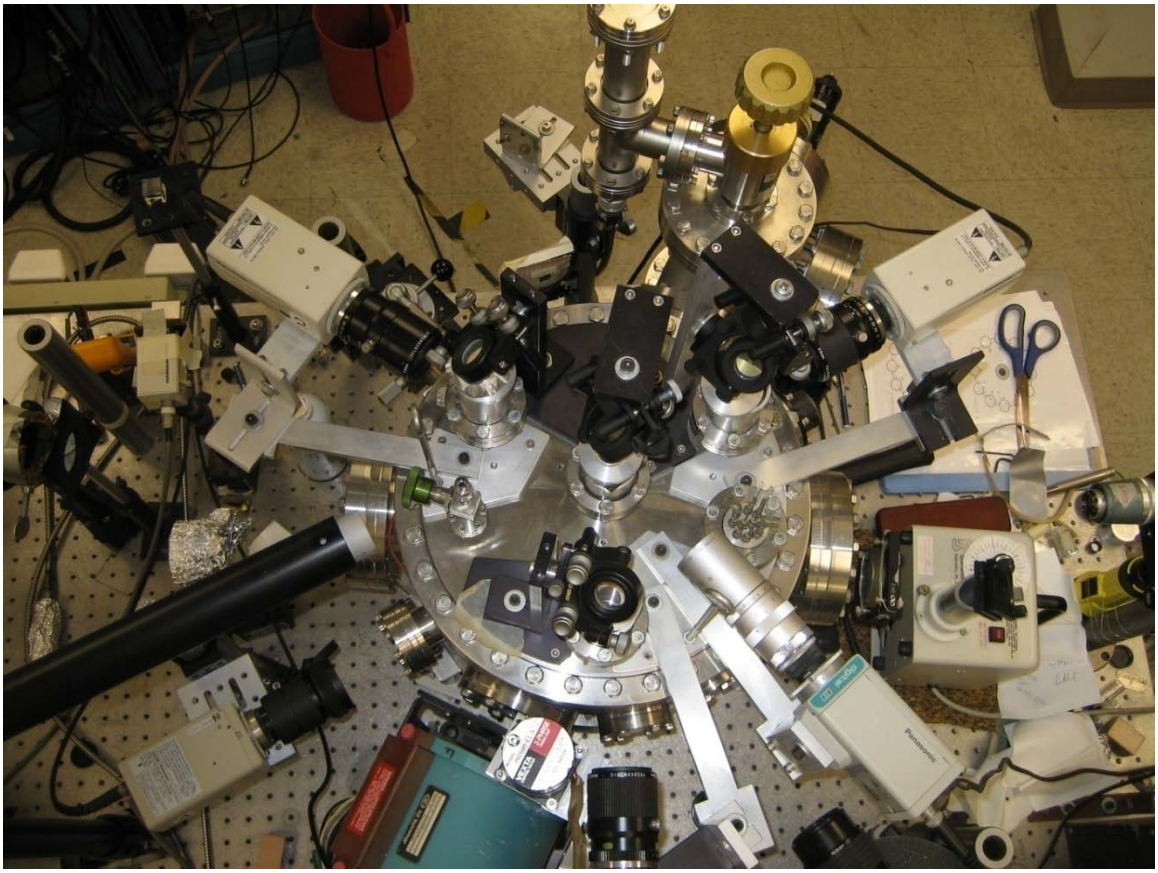

Figure 2.3: Top View of ESL at Caltech

2.2.2 Heating the sample

Sample heating is achieved by using a 200 Watt YAG laser. To further improve the uniformity of the sample temperature a tetrahedral laser heating arrangement was developed and implemented to the ESL system [7]. Uniform sample temperature means reduced temperature gradient across the sample. This translates to reduced thermal induced density gradients as well as surface tension gradients that are responsible for induced convective flows (Marangoni convection) in the sample. Such convective flows will affect the measurement results of physical properties, particularly transport properties such as atomic diffusion, thermal conduction, and viscosity [8]. For example, convective mixing can obliterate a diffusion profile making quantitative analysis difficult if not impossible.

A balanced heating method was also found to be important to prevent a volatile sample from being propelled by the action of vaporizing material. The symmetric tetrahedral heating arrangement made the measurements of thermophysical properties of Ti-6Al-4Vand Si-Ge alloys possible with increased accuracy [9]. These details are further described in Chapter 4 and Chapter 5.

As illustrated in Figure 2.4, where a sample is heated by a single laser beam, power input is asymmetrical with energy input on one side of the sample. Energy is lost by radiation over the entire sample. Under steady state conditions, the net power input and output are equal and a time independent temperature profile is achieved in the sample.

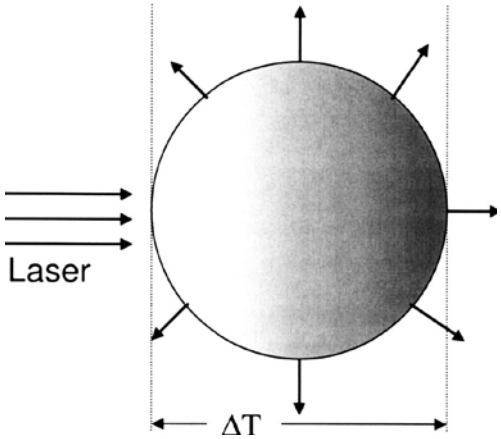

Figure 2.4: Schematic illustration of single beam heating by a laser beam and radiation loss by the sphere producing a temperature gradient

To obtain the exact steady state temperature distribution in the sphere, one solves the steady state Fourier equation (essentially Laplace's equation) for the boundary condition

$$J_r(R,\theta,\varphi) = -k\left(\frac{\partial T}{\partial r}\right)_{r=R} = \varepsilon\sigma_{SB}T_s^4 - P_{laser}(\theta,\varphi) \qquad (2.2)$$

where $J_r(R,\theta,\varphi)$ is the net radial component of the heat flux out of the sphere surface, k is the thermal conductivity of the sample, R is the sample radius, and $P_{laser}(\theta,\varphi)$ is the laser power input at the sphere surface.

The steady state heat flow equation in a sphere is a solution to the Laplace equation and can be solved by expanding temperature T in spherical harmonics Y_{lm}:

$$T(r,\theta,\varphi) = \sum_{l=0}^{\infty}\sum_{m=-l}^{+l} A_{lm}\frac{r^l}{R^l}Y_{lm}(\theta,\varphi) \Rightarrow \nabla^2 T = 0\,. \qquad (2.3)$$

The coefficients A_{lm} in the expansion are to be determined from the boundary condition that the heat flow from the surface equals the net radiated power density p (laser input power minus Stephen-Boltzmann radiation heat loss).

$$\kappa\vec{\nabla}T\cdot\vec{n}\Big|_{surface}=\kappa\sum_{l=0}^{\infty}\sum_{m=-l}^{+l}A_{lm}\frac{lr^{l-1}}{R^{l}}Y_{lm}(\theta,\varphi)\Big|_{r=R}=p$$
$$\Rightarrow A_{lm}=\frac{1}{\kappa}\frac{R}{l}\oiint_{4\pi}Y_{lm}^{*}\,p\,d\Omega. \qquad (2.4)$$

This net radiated power density includes laser heating and Stephen- Boltzmann radiative cooling.

Calculations have been done for the single-beam (polar) and tetrahedral four-beam case, with the beam(s) focused to a point or uniformly spread over an entire hemisphere, for sample sizes of R=1 mm and R=6.35 mm. A T302 stainless steel ball with a thermal conductivity of k =16.7 W/m K (at 1000 K) and a total hemispherical emissivity of ε =0.3 was considered as a test case.

For comparison, the bulk metallic glass-forming alloy $Zr_{58}Nb_3Cu_{16}Ni_{13}Al_{10}$ (Vit106a) was chosen, with ε =0.26 and k =25 W/m K (at 1000 K). Three different temperatures were considered, representative of the entire undercooled liquid region: 960 K, above the crystallization nose of the TTT diagram, 900 K, at the nose, and 740 K, below the nose. The results are summarized in Table 2.1, which gives the maximum temperature variation over the sphere under steady state heating conditions.

Table 2.1: Calculated temperature variation from the leading term in the spherical harmonic expansion reflecting the maximum temperature variation over the sample for $Zr_{58}Nb_3Cu_{16}Ni_{13}Al_{10}$ (Vit106a) samples of 1 mm in radius and a stainless steel ball with a radius of 6.35 mm heated with different heating geometries

Sample	Radius of Spheres (10^{-3} m)	Average temperature (K)	1 beam focused (K)	1 beam spread out (K)	4 beam focused (K)	4 beam spread out (K)
Vit106a	1	960	3.1	2.1	1.3	0.055
		900	2.4	1.6	1	0.043
		740	1.1	0.7	0.47	0.02
SST 302	6.35	960	33.7	22.5	14.1	0.59
		900	26	17.3	10.9	0.46
		740	11.9	7.9	4.9	0.21

The experimental setup to divide a single YAG laser beam into 4 equal intensity beams is illustrated in Figure 2.5, where three 50/50 beam splitters and three mirrors are used. The use of beam splitters to divide the single laser beam into four beams eliminates the uncorrelated fluctuations in power, which would arise if separate lasers were used.

With the present setup the laser power drift will only affect the average temperature but will not induce variations in temperature gradients (such as dipole, quadruple, etc.).

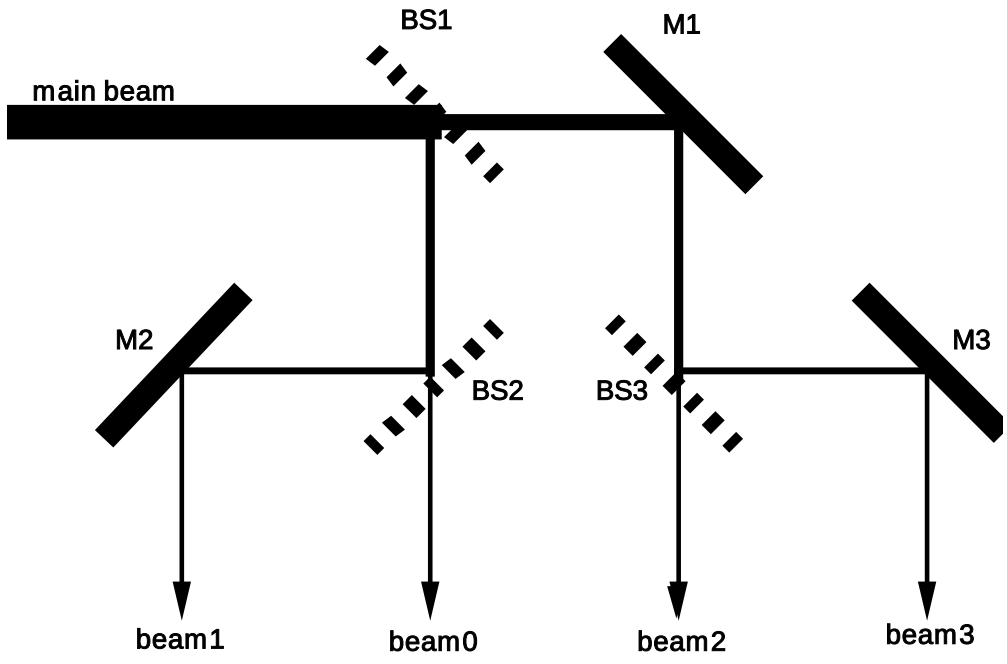

Figure 2.5: Schematic illustration of the equalization of four laser beams originated from one laser. Three beam splitters 50/50 and three mirrors were used to divide the main laser beam into four beams of roughly equal power

As in Figure 2.5, our setup of the optical system was mounted on the top flange of a vacuum chamber in such a way that three of the four vertical beams went through three windows that are located at the apexes of a equilateral triangle and the fourth beam went through a window that was located at the center of the triangle. The electrode assembly was so positioned in the chamber that the central beam irradiated the top of the sample while the three side beams were directed to the sample through mirrors. All the optical components are arranged in such a way that the four beams irradiate the sample satisfying a tetrahedral geometry as illustrated in Figure 2.6.

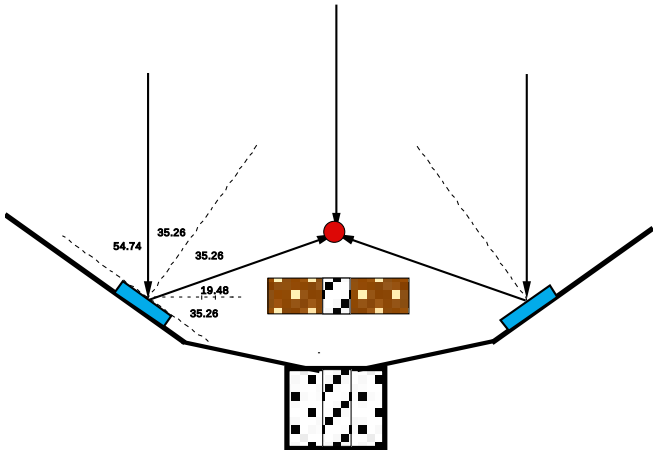

Figure 2.6: Schematic illustration of tetrahedral laser radiation setup

2.2.3 Tetrahedral laser heating and verification of temperature gradients reduction

In order to verify the predicted reduction of temperature variations over the sample, a T302 stainless steel ball, 6.35 mm in radius, with thermal conductivity of 16.7 W/m K was used. The relatively large sample size enhanced temperature variations and facilitated attaching thin thermocouples. The sample was suspended by four thin wires.

Four thermocouples were connected to the sample's surface as shown in Figure 2.7. They were positioned in such a way that they detected the maximum temperature variations in the sample. Thermocouples Tc1 and Tc3 were utilized to measure the maximum temperature variations for the one-beam case and Tc2 and Tc4 for the maximal temperature variation in the four-beam case. Tc2 is located in the middle of the triangle formed by the laser spot 1, 2, and 3. K-type thermocouples of 0.07 mm in diameter were used and similar wires were used to support the sample. The temperature gradients were measured after the sample was allowed to reach steady state. For calibration purposes, the characteristics of different thermocouples were tested in a uniform 1100 K temperature field established by a resistant furnace. Their temperature readings varied less than 0.7 K.

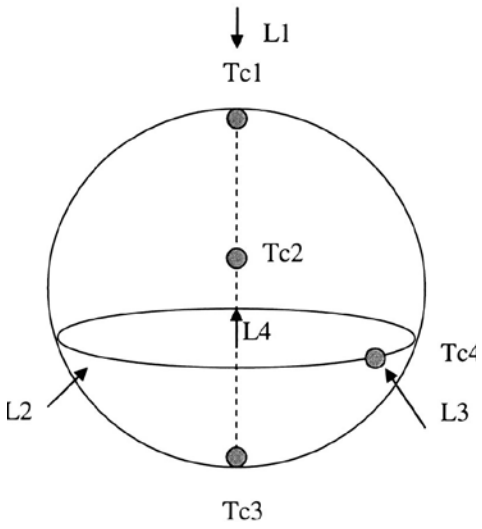

Figure 2.7: Schematic illustration of the positions where the thermocouples were attached (shown by circle) and the spots where the laser beams impinged on the sample (→). For the one-beam case, *L*1 was used and the maximum temperature variations for this case were measured by Tc3 and Tc1

Figure 2.8 (a) shows the measured maximum temperature variations over the sample for a sample that was heated by a single laser beam. When the beam was focused on the sample to a spot of about 1.6 mm in diameter, the temperature variation on the sample was as much as 35 K for an average sample temperature of 980 K. If the beam was spread out to about 10 mm in diameter (diffuse beam) the temperature variation went down to 10.4 K at the average temperature 943 K. When the sample was heated by four focused laser beams in a tetrahedral geometry as shown in Figure 2.8(b), the temperature variation still was as high as 22 K at an average temperature of 1003 K. However, as soon as the four beams in the tetrahedral geometry were spread out, the temperature variation was dramatically decreased to less than 0.5 K at an average sample temperature of 1003 K. This temperature variation was in the range of the experimental error of 0.7 K. Also shown in Figure 2.8 is the amplitude of the temperature variations calculated according to Eq. (2.3) in which only the leading term was considered. An emissivity of 0.3 was used for the calculations. Since the maximum temperature variations scale linearly with the samples radius, Figure 2.8 can be used to extrapolate the temperature variations for different sample sizes.

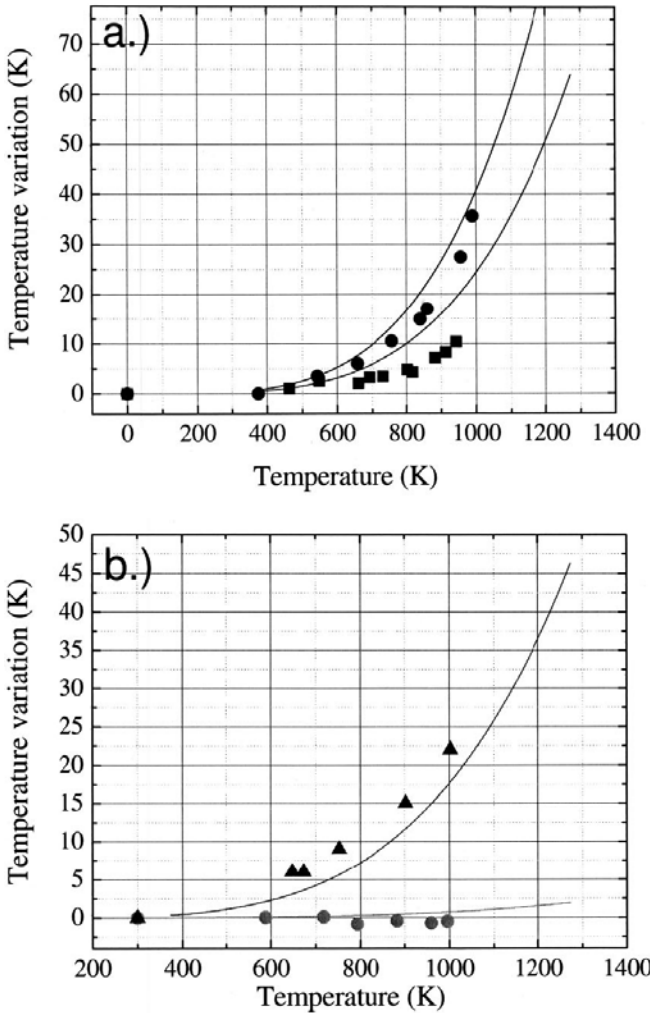

Figure 2.8: Temperature variations within the sample for:

(a) 1-beam heating geometry [focused beam (solid circle) diffusive beam (solid square)]

(b) 4-beam heating geometry [focused (solid triangle) and diffuse (solid circle)]. The solid curves resulted from the calculations according to Eq. (2.3).

2.3 Conclusion

Instrumentation on the Caltech ESL to upgrade the heating system has been carried out; a theoretical model was used to predict sample temperature variation under steady state heating by laser beams. This model was compared with experiments.

The advantage of the improved laser heating with the tetrahedral arrangement is the reduced temperature gradient across a liquid sample, which tends to create density gradients and surface tension gradients that are responsible for inducing convective flows in the sample. Such convective flows will affect measurement results of physical properties, particularly transport properties such as atomic diffusion, thermal conduction, and viscosity. Convective mixing can completely obscure diffusion profiles for both heat flow and atomic diffusion. Reduction of sample temperature gradients is thus a substantial improvement in the ESL platform.

Another advantage of the tetrahedral heating arrangement is the improvement of stability for a levitated volatile sample at high temperature. During the heating period, four equally powered laser beams keep the sample at a predetermined position instead of pushed away from it by imbalanced force field. Such an arrangement allowed the thermophysical properties of Ti-6Al-4Vand Si-Ge alloys to be measured quickly with increased accuracy.

2.4 References

[1] W. K. Rhim, K. Ohsaka, P. F. Paradis, and R. E. Spjut, Review of Scientific Instruments 70, 2796 (1999).

[2] D. Li and D. M. Herlach, Europhys. Letter 34, 423 (1996).

[3] C. Landron, L. Hennet, P. Berthet, J. P. Coutures, and J. F. Berar, 1999), p. 87.

[4] F. Babin, J. M. Gagne, P. F. Paradis, J. P. Coutures, and J. C. Rifflet, Microgravity Science and Technology 7, 283 (1995).

[5] P. von Kampen, U. Kaczmarczik, and H. J. Rath, (Pergamon-Elsevier Science Ltd, 2006), p. 278.

[6] W. K. Rhim, S. K. Chung, D. Barber, K. F. Man, G. Gutt, A. Rulison, and R. E. Spjut, Review of Scientific Instruments 64, 2961 (1993).

[7] J. Schroers, S. Bossuyt, W. Rhim, J. J.Z. Li, Z. Zhou, and W. Johnson, Review of Scientific Instruments 75, 4523 (2004).

[8] S. Bossuyt, J. Schroers, W. Rhim, and W. Johnson, Review of Scientific Instruments 76 (2005).

[9] J. J.Z. Li, W. Johnson, and W. Rhim, Applied Physics Letter 89 (2006).

3 Non-contact Diagnostic Methods Based on ESL for Thermophysical Properties Measurement

3.1 Volume Measurement

The volume of a levitated sample is measured from the backlit sample images taken by a high-resolution high-speed CCD camera. During the heating and cooling process the light radiated by the sample will change in both intensity and color, which makes it difficult to define the boundary of the sample. To overcome this difficulty, we have used a backlit image created by violet-colored light by putting a violet filter in front of the camera and another one behind the UV lamp. For the temperature range we are measuring, we have been getting well defined boundaries between the sample and the background.

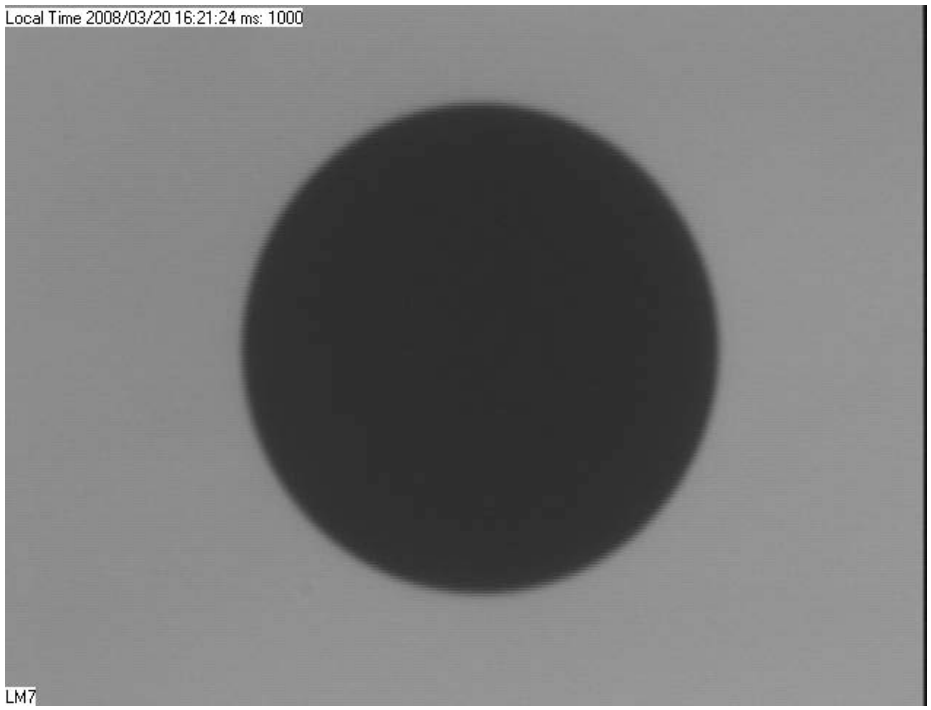

Figure 3.1: Backlight image of a molten Vit1 sample levitated in an ESL

Since the shape of the molten sample levitated by ESL is axisymmetric around the vertical z-axis when not rotating, taking a single side image of the sample is sufficient to extract full volume information from it. Figure 3.1 shows a typical image of a molten sample so obtained. The recorded video images are digitized and the sample volume is extracted from each video frame by fitting the image with Legendre polynomial. Real sample volumes were obtained by comparing the volumes with that of a calibration ball.

Thermal expansion coefficient is calculated as:

$$\alpha = \frac{1}{V}\frac{\partial V}{\partial T} \tag{3.1}$$

A detailed analysis has shown accuracy of 0.8% for density and 0.2% for the thermal expansion coefficient [1].

3.2 Temperature Measurement

For sample temperature measurements we have used a two-color pyrometer (from Mikron Infrared Inc, Model: MI-GAR12-LO). This pyrometer is capable of measuring temperature in the range 500 ℃ to 2200 ℃. For temperatures higher than 2200 ℃ or lower than 500 ℃, we can use the single-color mode of the pyrometer with emissivity calibration. Results from the pyrometer are calibrated using the liquidus temperature of the sample that is available in the literature, or one independently measured, for example, by a differential scanning calorimeter.

3.3 Surface Tension and Viscosity Measurements

The surface tension and the viscosity are measured by oscillating the sample with a pulse of AC voltage in the vertical direction at the frequency of harmonic oscillation of the sample. The amplitude of the oscillation of the sample is measured by projecting a laser beam at the sample and having a photo detector measure the intensity of laser beam which goes through a vertical slide at the center of the sample image. This is illustrated in Figure 3.2 and the intensity can be expressed as,

$$I = a + b * e^{t/\tau} * \sin(\omega t + \varphi) \qquad (3.2)$$

where *a* is a constant, *b* is proportional to the maximum of oscillation amplitude, *t* is the time, τ is the decay time constant, ω is the resonant frequency, and φ is a constant phase

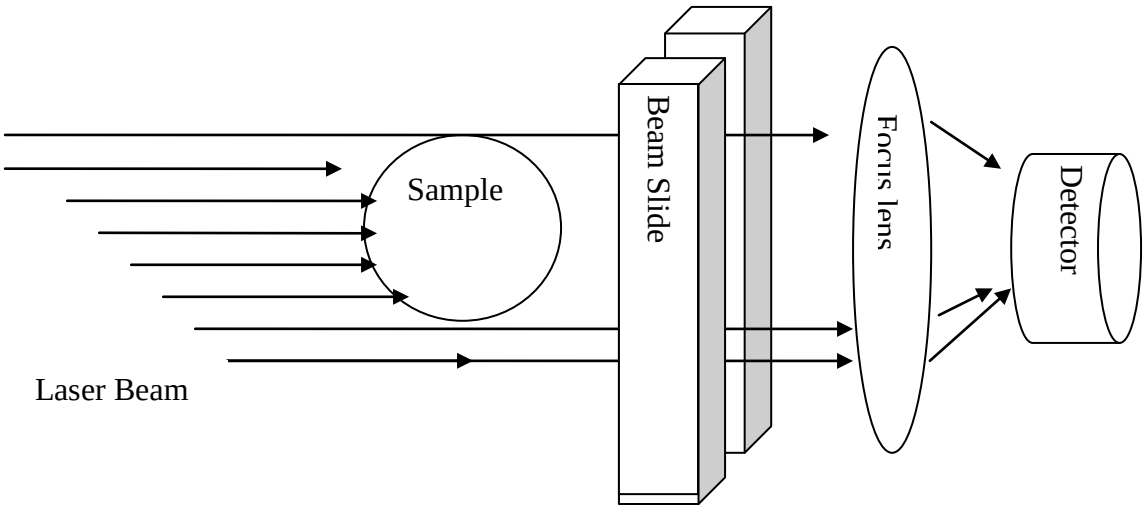

Figure 3.2: Illustration of measurement of vertical oscillation amplitude of a molten sample

factor. Through Fast Fourier Transformation (FFT) analysis, both the oscillation frequency ω and the amplitude decay constant τ can be determined. The surface tension σ is determined by the equation [2],

$$\omega^2 = \frac{8\sigma}{\rho r^3}\left(1 - \frac{Q^2}{64\pi^2 r^3 \sigma \varepsilon_0}\right) \tag{3.3}$$

where Q is the charge on the surface, r is the radius of the drop, ρ is the density, and ε_0 is permittivity. Viscosity can be calculated by,

$$\eta = \frac{\rho r^2}{5\tau}. \tag{3.4}$$

The key to a successful measurement of viscosity is to have a stable levitation with rotation only along the z-axis. A detailed description was given in elsewhere [2] and a typical result of oscillation is illustrated in Figure 3.3.

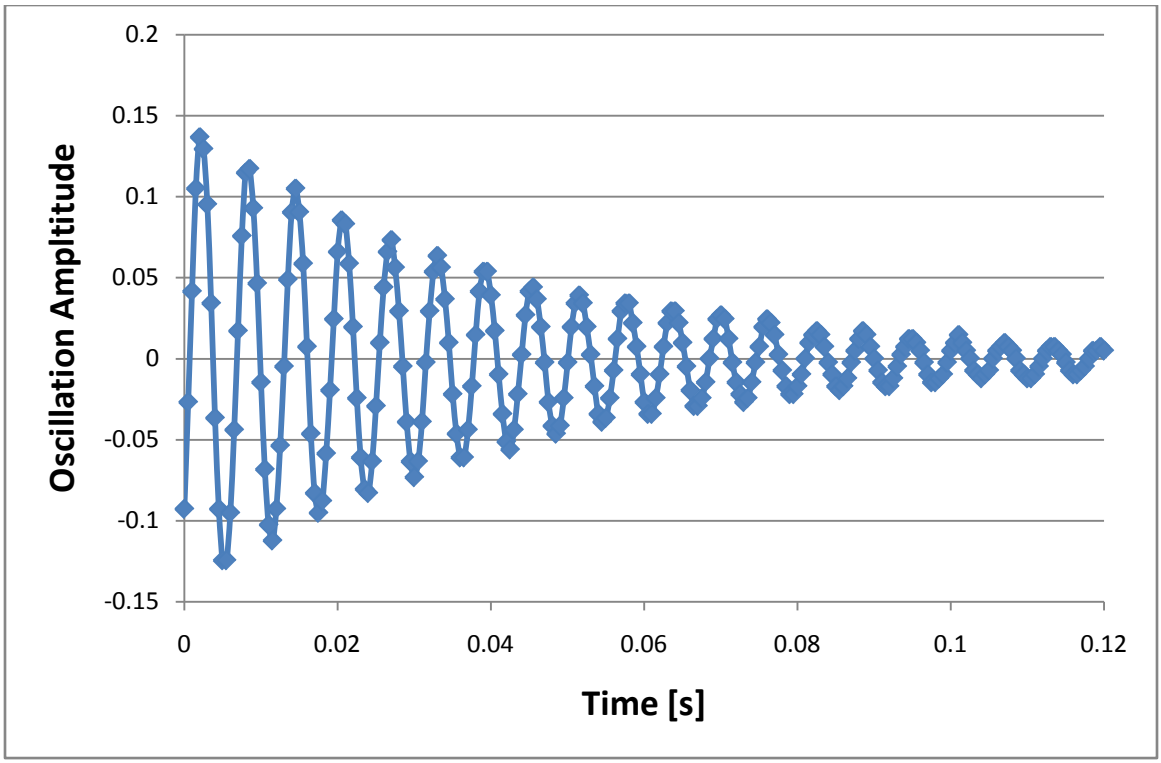

Figure 3.3: Oscillation of a molten Vit 1 at temperature 1022 ℃

3.4 Specific Heat and Total Hemispherical Emissivity

When the heating laser is turned off, the cooling of a levitated spherical liquid sample will follow the Stephen-Boltzmann equation for pure radiative cooling,

$$mC_p \frac{dT}{dt} = -4\pi r^2 \varepsilon \sigma_{SB} \left(T^4 - {T_0}^4\right) \qquad (3.5)$$

where mC_p is the heat capacity, σ_{SB} is the Stephen-Boltzmann constant, ε is the total hemispherical emissivity, T is the sample temperature and T_0 is the room temperature.

From the radiative cooling curve, we can calculate C_p/ε as a function of temperature T. If either one of C_p or ε is available from data, the other can be calculated [3]. A good example is the measurement of Ti-6V-4Al, which is discussed in Chapter 4.

3.5 Time-Temperature-Transformation (T-T-T) Curves for Crystallization

In the research of crystallization process, T-T-T curve is important to understand crystallization both in thermodynamics and kinetics. The ideal T-T-T curve is supposed to be measured by cooling the sample to a certain temperature at an infinite cooling rate and holding the temperature while measuring the fraction of crystallization at different times. Practically it is difficult to measure the TTT curve of molten metallic materials because it requires a containerless process and long time of measurement.

The first TTT curve of BMGs was measured by Kim *et al.* who used the original model of this ESL [4]. As illustrated in Figure 3.4, a molten levitated sample is cooled radiatively from above melting temperature to a predetermined temperature. A

predetermined power of laser is turned on to maintain a constant temperature. The recalescence of a liquid sample marks the initiation of crystallization.

The limitation of measuring T-T-T curve by ESL is the slow radiative cooling rate. So far, only a few TTT curves of BMG alloys have been measured by ESL [5].

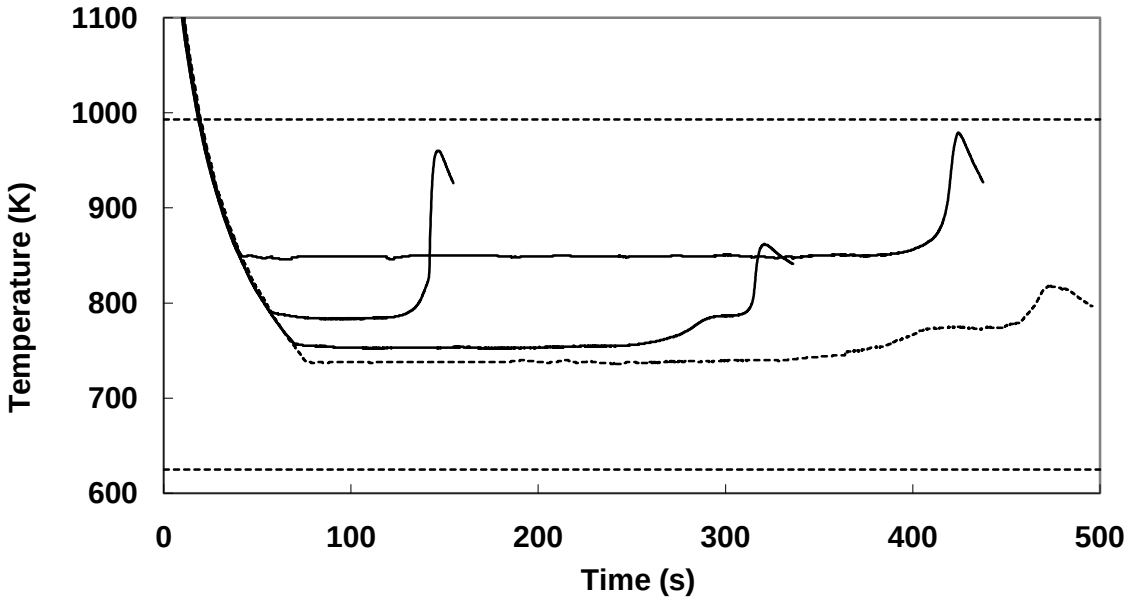

Figure 3.4: Measurement of T-T-T curve by ESL

3.6 References

[1] S. K. Chung, D. B. Thiessen, and W. K. Rhim, Review of Scientific Instruments **67**, 3175 (1996).

[2] W. K. Rhim, K. Ohsaka, P. F. Paradis, and R. E. Spjut, Review of Scientific Instruments **70**, 2796 (1999).

[3] A. J. Rulison and W. K. Rhim, Review of Scientific Instruments **65**, 695 (1994).

[4] Y. Kim, R. Busch, W. Johnson, A. Rulison, and W. Rhim, Applied Physics Letter **68**, 1057 (1996).

[5] S. Mukherjee, J. Schroers, W. Johnson, and W. Rhim, Physical Review LETTERS **94** (2005).

4 High Temperature Thermophysical Properties of Molten Ti-6Al-4V

4.1 Abstract

Thermophysical properties of both solid and liquid Ti-6Al-4V alloys were measured around the melting temperature by ESL. The properties include the specific heat, the total hemispherical emissivity, the heat of fusion, the density and the thermal expansion coefficient. Liquid properties were also measured over 280 K of undercooled region. Over 1661 K~ 1997 K the ratio of the constant pressure heat capacity and the total hemispherical emissivity for liquid phase can be expressed by $C_{P,\,l}/\varepsilon_{T,\,l} = 3064 + 0.1291(T - T_m)$ J/kg/K with the melting temperature T_m = 1943 K. For solid phase it can be expressed by $C_{P,S}/\varepsilon_{T,S} = 2699 + 0.08191(T - T_m)$ J/kg/K over 1200~1943 K. The heat of fusion has been calculated to be 300 kJ/kg. Liquid density over 1661 to 1997 K can be expressed by $d_l(T) = 4123 - 0.254\,(T - T_m)$ kg/m^3, and the corresponding volume expansion coefficient is $\alpha_l = 6.05 \times 10^{-5}$ K^{-1} near T_m.

4.2 Introduction

Ti-6Al-4V and its variants are widely used for industrial applications such as turbine blades, air-frames, rocket components, ship propeller shafts, pressure vessels, prosthetic implants, automotive components and sports equipment. Such wide applications are due primarily to their low density, good strength, ductility, refractory nature, and their resistance to corrosive chemical environments (acids, chloride solutions, sea water, etc.) [1]. While thermophysical data of Ti-6Al-4V in both liquid and solid phases are essential

for simulation of the casting and modeling of crystallization phase transition, the high melting point and the risk of contamination in its molten phase make it difficult to measure its thermophysical properties in liquid state using traditional methods This makes it necessary to use a containerless technique. In the present work we attempted to use the ESL along with the accompanying non-contact diagnostic techniques for determination of thermophysical properties of Ti-6Al-4V [2-4]. Our experimental facility allowed us to levitate the sample in high vacuum, thus isolating it from container walls as well as surrounding gasses [5].

Some of the thermophysical properties of Ti-6Al-4V have been published by other authors. Kaschnitz *et al.* used pulse heating method to measure C_P and electrical resistivity of both solid and liquid [6]. However, their liquid data are limited to above the melting temperature. Brooks *et al.* used scanning calorimetry at lower temperatures and the drop in calorimetry at high temperature to measure enthalpy [7]. The ESL data obtained complement some of these existing data with more detail information in the undercooled temperature region. In the ESL, the liquid Ti-6Al-4V revealed undercooling as much as 282K. Properties presented in this thesis are specific volume, density, thermal expansion, specific heat capacity, heat of fusion, enthalpy and Gibbs free energy difference between undercooled liquid and solid. Using the solid phase specific heat measured by Kaschnitz *et al.* and C_P/ε_T measured by the ESL, we also determined total hemispherical emissivity in the solid phase.

4.3 Experiment Details

The Ti-6Al-4Vsamples provided by the United Technology Corporation were ground to roughly spherical shape in diameter about 2.5 mm. Sample temperature was measured using a single color pyrometer operating at 700 nm and it was calibrated with respect to the known melting temperature T_m =1943 K. Upon blocking the heating laser beams, both the sample temperature and the sample video-images were simultaneously recorded. Since the molten sample levitated by the ESL is axisymmetric around the vertical direction in absence of a sample rotation, a single side image of the sample contains full volume information. The recorded video images are digitized and the sample volume is extracted from each video frame by fitting the image with Legendre polynomial [4]. Knowing the mass of the sample, the density is calculated.

4.4 Results and Discussion

4.4.1 Specific heat

Figure 4.1 shows that the liquid Ti-6Al-4V cooled from 1977 to 1661 K with 282 K undercooling before it recalesced to T_m and turned into a α phase solid. The α phase solid kept cooling until an α to β transition took place.

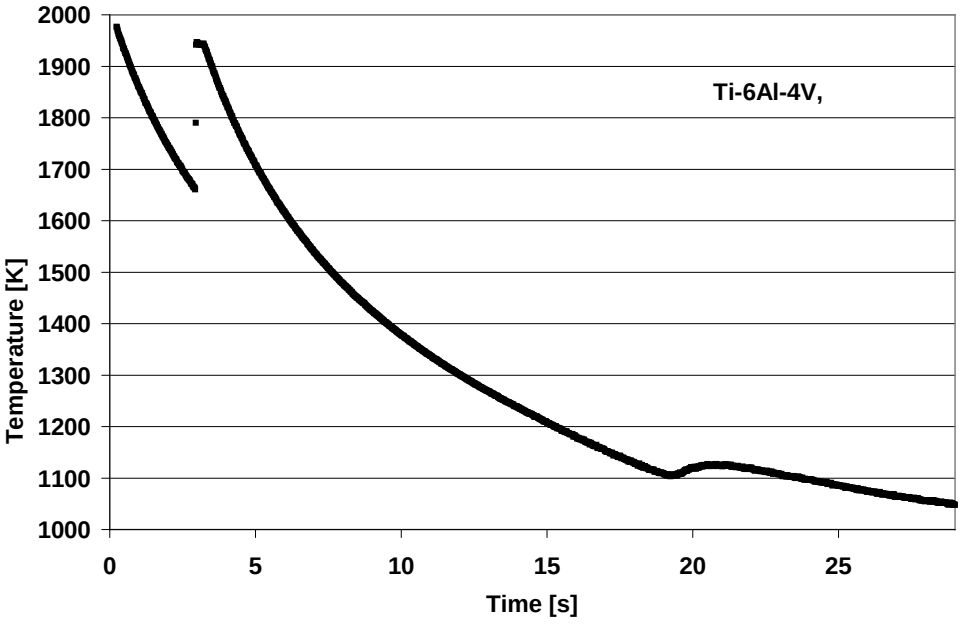

Figure 4.1: Free cooling curve of a Ti-6Al-4V sample in absence of heating beams. Note that the liquid exhibits a deep undercooling before the recalescence. Also note an α to β phase transition taking place in solid phase

The ratio between the constant-pressure heat capacity and the total hemispherical emissivity as a function of the temperature was calculated from Eq. (3.4) in which *dT/dt* was obtained from the Figure 4.1. These results are shown in Figure 4.2 for both the solid and the liquid phases. For the liquid phase, $C_{P,l}/\varepsilon_{T,l}$ can be expressed by:

$$\frac{C_{p,l}}{\varepsilon_{T,l}} = 3064 + .1291(T - T_m)\ [J/kg/K], \text{ over } 1661\ K \leq T \leq 1977\ K. \qquad (4.1)$$

Our results for solid $C_{P,S}/\varepsilon_{T,S}$ can be expressed by:

$$\boldsymbol{C_{P,S}/\varepsilon_{T,S}} = 2699 + 0.08191(T - T_m)\ [J/kg/K] \text{ over } 1200K \leq T \leq 1943K. \qquad (4.2)$$

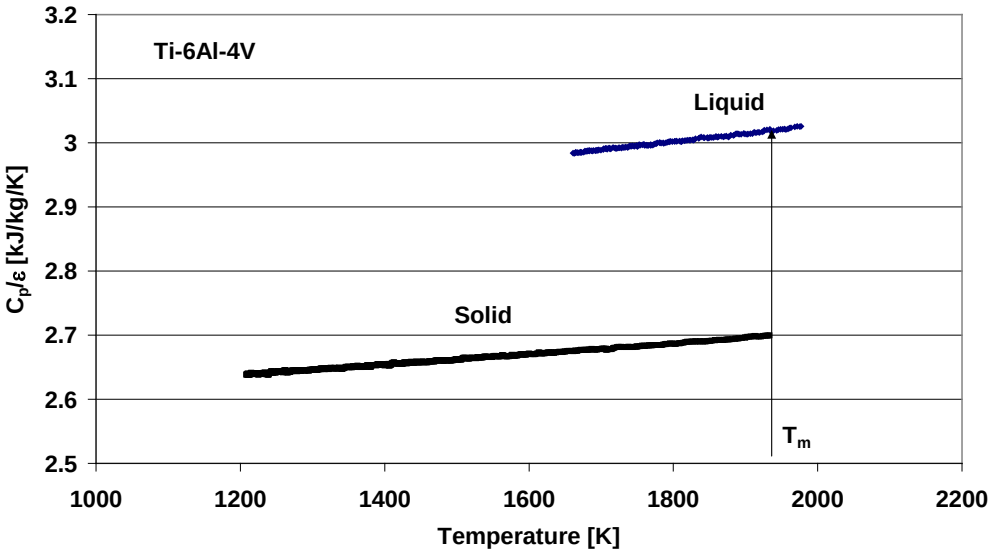

Figure 4.2: Ratio between the constant-pressure heat capacity and the total hemispherical emissivity of both liquid and solid Ti-6Al-4V as a function of temperature

From this equation (4.1) one can determine $\varepsilon_{T,l}$ if $C_{P,l}$ is known, or vise versa. If we use the value $C_{P,l}$ = 931 J·kg^{-1}·K^{-1} at T_m given by Kaschnitz *et al.* [6], the hemispherical total emissivity $\varepsilon_{T,l}$ is determined to be $\varepsilon_{T,l}$ = 0.304. If we assume $\varepsilon_{T,l}$ =0.304 to remain unchanged over a few hundred degrees around the melting temperature, $C_{P,l}$ can be determined using Eq. (4.1) and it is expressed by:

$C_{P,l} = 931+0.0392(T-T_m)$ *[J/kg/K]* over 1661 K≤ T ≤ 1977 K. (4.3)

Kaschnitz *et al.* independently measured $C_{P,S}$ for solid phase [6] using the drop calorimetric technique. In Figure 4.3, their $C_{P,S}$ results for solid phase along with our results for liquid phase in Eq. (4.3) are shown.

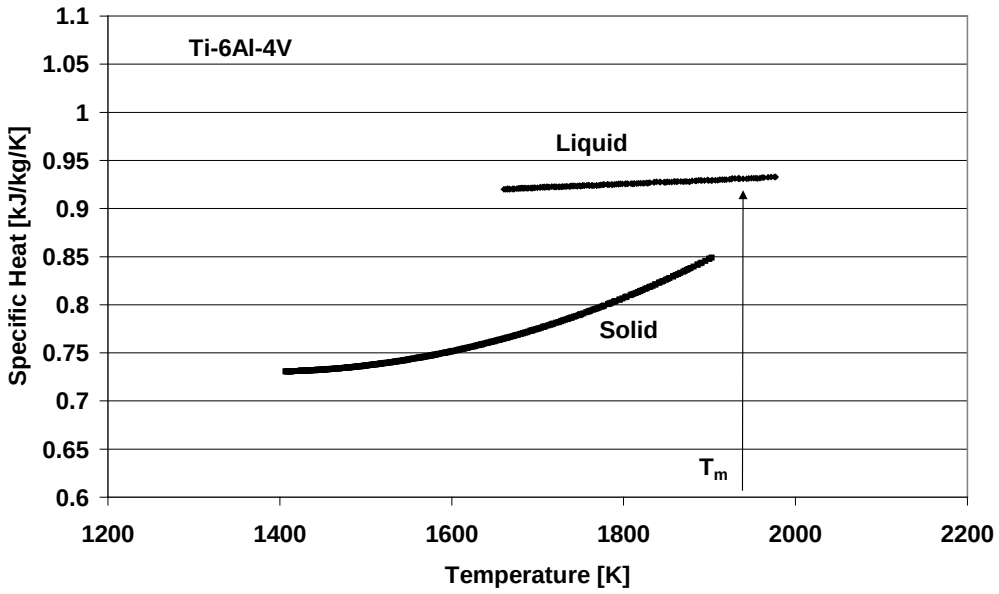

Figure 4.3: Constant pressure specific heat of both liquid and solid Ti-6Al-4V. The liquid data are from our experiment and solid data are from Kaschnitz *et al.* [6] who used the drop calorimetric technique

4.4.2 Enthalpy and Gibbs free energy

The heat of fusion can be determined by adding the enthalpy contributions of the undercooled liquid and that of the isothermal region following the recalescence (see Figure 4.1). The contribution of the undercooled portion was obtained by integrating $C_{P,l}$ over the temperature range between T_m and the maximum undercooling temperature, whereas that of the isothermal region following the recalescence was obtained by integrating $\varepsilon_{T,l} A\sigma_{SB} (T_m^4 - T_a^4)$ over that region. The sample surface area was derived from the measured specific volume data given below. The heat of fusion so obtained was 300 kJ kg^{-1}, which agrees well with 295 ± 15 kJ/kg measured by Brooks *et al.* [7], and 286 ± 17 kJ/kg by McClure and Cezairliyan [9].

Utilizing the values that are given above, the difference of enthalpy between liquid and solid phases can be calculated by:

$$\Delta H_{l-s}(T) = \Delta H_m + \int_{T_m}^{T} \Delta C_p^{l-s}(T')dT'$$

$$= 300 + 6.81x10^{-2}(T - T_m) - 1.66x10^{-4}(T - T_m)^2 \ [kJ/kg/K], \qquad (4.4)$$

where ΔH_m =300 kJ kg^{-1} is the enthalpy of fusion, and $\Delta C_p^{l-s}(T)$ the specific heat difference between liquid and solid.

Likewise, the Gibbs free energy difference between liquid and solid phases can be calculated by:

$$\Delta G_{l-s}(T) = \Delta H_m + \int_{T_m}^{T} \Delta C_p^{l-s}(T')dT' - T[\Delta S_m + \int_{T_m}^{T} \frac{\Delta C_p^{l-s}(T')dT'}{T'}]$$

$= - 1.57x10^{-1}(T-T_m)-3.30x10^{-5}(T- T_m)^2$ [kJ/kg/K] (4.5)

4.4.3 Specific volume

The specific volume of Ti-6Al-4V was measured in the temperature range from 1050 to 1943 K for solid and from 1661 to 1977 K for liquid. The results are graphically presented in Figure 4.4. The liquid specific volume exhibits a linear nature and its least-squares fit to the data can be expressed by:

$V_l = V_{m,l}\,[1+ 6.05x10^{-5}(T - T_m)]$ [m^3/kg] over 1661 K ≤ T ≤ 1977 K, (4.6)

where $V_{m,l}$ =2.425x10^{-4} m^3/kg is the specific volume at T_m, and 6.05x10^{-5} K^{-1} represents the volume thermal expansion coefficient of liquid Ti-6Al-4V at the T_m.

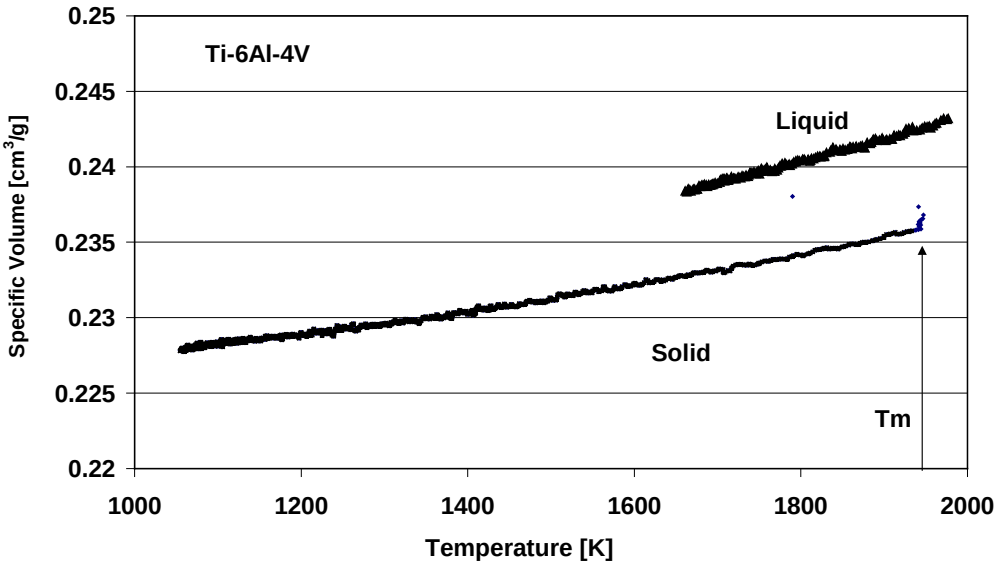

Figure 4.4: Specific volume versus the temperature of liquid and solid Ti-6Al-4V

4.4.4 Density

The sample density derived from the measured specific volume is shown in Figure 4.5. The liquid density can be fitted by:

$$d_l = 4122 - 0.2535(T - T_m), [Kg\ m^{-3}]$$

$$over\ 1661\ K \leq T \leq 1977\ K \qquad (4.7)$$

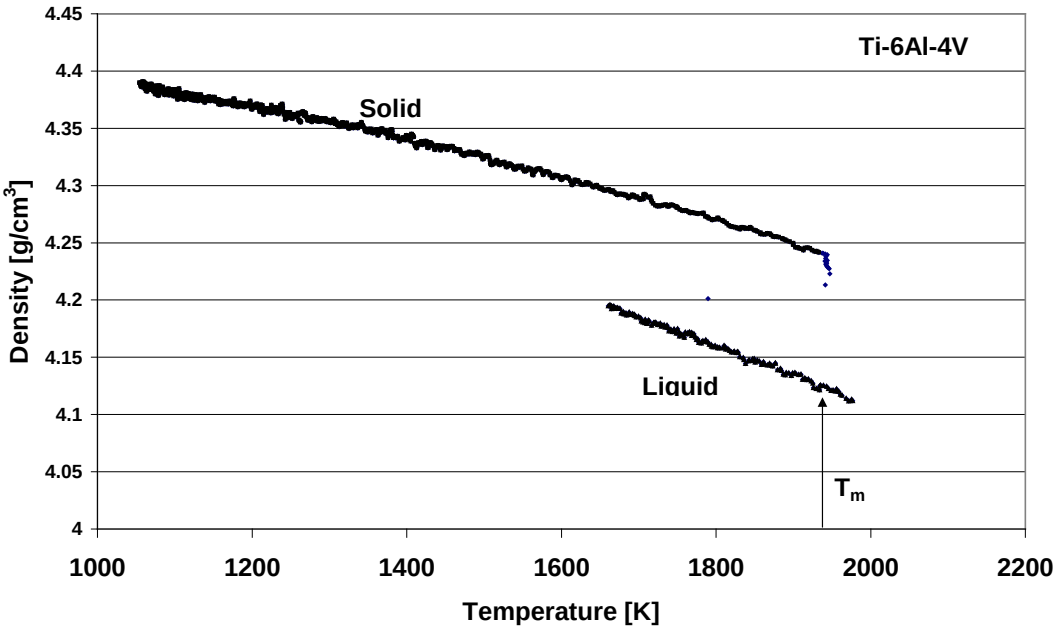

Figure 4.5: Density of Ti-6Al-4V in both liquid and solid state

4.5 Discussion

The accuracy of the measurements was estimated to be ±0.5%. Even though we could measure the volume with 0.5% of accuracy, we found that the mass change during the melting can affect the accuracy of the density, specific volume and the composition. To reduce such error by mass loss of Al in Ti-6Al-4V, we kept the sample in molten state for a very short time (~6 seconds) before we turned the heating laser off and let the sample cool radiatively. Both the initial mass and the final mass of the sample were measured and we used the final mass to calculate the density to match the volume data that we measured during the final cooling. The mass of the Ti-6Al-4Vsample was changed from

32.8mg to 32.6 mg during the melting process. Consider the mass loss of about 0.5 % during the cooling and 0.5% during the heating; we estimate the total accuracy of specific volume and density to be 1%, which excludes the uncertainty in temperature. Assuming that 1% of mass loss is from the evaporation of aluminum, the final composition could be shifted to 92Ti4Al4V. Since the emissivity of solid is not a constant for the temperature we measured, the temperature on the solid in Figure 4.1 and Figure 4.2 are for illustration only until more information on the emissivity available.

Data comparison with pure titanium [10] is summarized in Table 4.1. We found that molten titanium and molten Ti64 have the same melting temperature (1943 K), and almost the same specific volume but their thermal expansion coefficients are quite different. The thermal expansion coefficient of molten Ti-6Al-4V is only 52% that of molten titanium.

Table1 4.1: Density Comparison of Ti-6Al-4Vwith Titanium in Liquid State at T_m

Material	T_m	Density [kg·m^{-3}]	Thermal Expansion Coefficient (K^{-1})	References
Molten Titanium	1943K	4321	1.17x10^{-4}	Paradis *et al.* [8]
Molten Ti-6Al-4V	1943K	4122	6.05x10^{-5}	Current study

4.6 Conclusion

A containerless measurement of Ti-6Al-4Vwas conducted by ESL in the temperature range of 1200 to 1977 K including 282 K of undercooling from liquidus temperature. Taking advantage of capabilities that are specific to ESL we have measured the ratio of specific heat and total hemispherical emissivity both in liquid and solid phases, the specific volume, and the density. The enthalpy of fusion extracted from our experiment agrees well with the literature values. The enthalpy and Gibbs free energy difference between liquid and solid that we calculated can be used for modeling and simulations.

4.7 References

[1] J.K. Wessel , *The Handbook of Advanced Materials*, (Wiley Interscience, 2004).

[2] W. K. Rhim, S. K. Chung, D. Barber, K. F. Man, G. Gutt, A. Rulison, and R. E. Spjut, Review of Scientific Instruments **64**, 2961 (1993).

[3] A. J. Rulison and W. K. Rhim, REVIEW OF SCIENTIFIC INSTRUMENTS **65**, 695 (1994).

[4] S. K. Chung, D. B. Thiessen, and W. K. Rhim, REVIEW OF SCIENTIFIC INSTRUMENTS **67**, 3175 (1996).

[5] J.J.Z. Li, W. Johnson, and W. Rhim, Applied Physics Letter **89** (2006).

[6] E. Kaschnitz, P. Reiter, and J.L. McClure, International. Journal of. Thermophysics, 23, 267-275 (2002).

[7] R. F. Brooks, J. A. J. Robinson, L. A. Chapman and M. J. Richardson, High Temp. High Pressures, 35/36, 193-198 (2003/2004)

[8] J. Schroers , S. Bossuyt , W. K. Rhim , J. J.Z. Li, Z. H. Zhou, W. L. Johnson, Review of Scientific Instrument 75 (11), 4523-4527 (2004).

[9] J. L. McClure and A. Cezairlian, International. Journal of Thermophysics, 13, 75-81 (1992)

[10] P. F. Paradis and W. K. Rhim, Journal of Chemical Thermodynamics **32**, 123 (2000).

5 Thermophysical Properties of Liquid Si_xGe_{1-x}

5.1 Abstract

Thermophysical properties of liquid Si_xGe_{1-x} (x= 0, 0.25, 0.5, 0.75, and 1) are measured by the ESL at Caltech. The specific volume, the density and the thermal expansion coefficient in full range of composition over a wide range of temperature are determined in liquid state. The viscosities of these liquid alloys are measured for the first time. The dependences of the liquid surface tensions on the temperature are measured for the first time.

5.2 Introduction

Semiconductors are playing important roles in our daily life today, and their thermophysical properties have been studied extensively. Silicon is the host material for the majority of semiconductor applications. The thermophysical properties of Si_xGe_{1-x} in crystalline, amorphous and liquid phases are of substantial interest. The atomic structure, electrical, optical and thermophysical properties of the liquid phase are the key factors that determine the quality of crystals grown from the melt. However, thermophysical properties of undercooled molten semiconductors have not been studied so much because molten semiconductors are highly reactive to the wall of the container. Several containerless methods have been applied to study molten Si and Ge [1--10], but only few studies have been reported on the alloys of Si_xGe_{1-x} [11--16]. Another interest in this study is to verify a first order liquid-to-liquid phase transition at roughly 1345K for undercooled Si. This was predicted by Angel and Borick [17].

In the present study of measuring the thermophysical properties of Si_xGe_{1-x} alloys in liquid state, a parallel effort has been formulated: one is to use the microgravity environment in an airplane as it flies through a parabolic trajectory in Europe [15], and the other is to use the ESL at Caltech for the same properties measurements. Such an effort provides valuable information about Si_xGe_{1-x} alloys. This is of great interest both in the academic as well as in the industrial community.

The previous studies on thermophysical properties of molten semiconductors by this ESL were limited within pure Si and Ge [7--9]. One of the new challenges to measure thermophysical properties of molten Si_xGe_{1-x} alloys is the evaporation of Ge atoms. The evaporating Ge changes the sample mass as well as the composition of the alloys. To overcome this problem, the mass loss must be monitored during the measurements. The ESL at Caltech, which is equipped with tetrahedral heating setup, enables us to conduct such quick measurements of molten Si_xGe_{1-x} in a high vacuum of 10^{-8} torr. The volume monitoring process allows us to track both the mass loss and the composition changes of the sample due to the evaporation simultaneously with the other property measurements.

5.3 Experimental Method

The high purity of 6N semiconductor Si_xGe_{1-x} (X=0, 0.25, 0.5, 0.75 and 1) samples used in our measurement were provided by Samwer. They measured the thermophysical properties of these samples in a microgravity environment provided by parabolic flights [15]. On our side at Caltech, the same setup of ESL as described in Chapter 2 has been used to measure the same properties. A special attention has been paid on the mass loss and composition shift during the experiment by checking the volume changes throughout

the experiments. Assuming the mass loss is due to the evaporation of Ge in Si_xGe_{1-x} alloys, we calibrated the data taking into account the mass loss and the composition shifts based on the monitored volume. This assumption is based on the higher vapor pressure of Ge in the temperature range of the measurements.

5.4 Result and Discussion

5.4.1 Specific volume and thermal expansion

Figure 5.1 shows the specific volume of liquid Si_xGe_{1-x} for x=0, 0.26, 0.55, 0.77 and 1, with a linear fit to the temperature:

$$v = a + bT \quad [cm^3/g] \qquad (5.1)$$

where $a = 8.66\times10^{-1}x^4 - 1.42x^3 + 7.79\times10x^2 - 8.70\times10^{-3}x + 1.58\times10^{-1}$ and $b = 6.78\times10^{-5}x^4 - 1.30\times10^{-4}x^3 + 8.52\times10^{-5}x^2 - 2.60\times10^{-5}x + 1.99\times10^{-5}$.

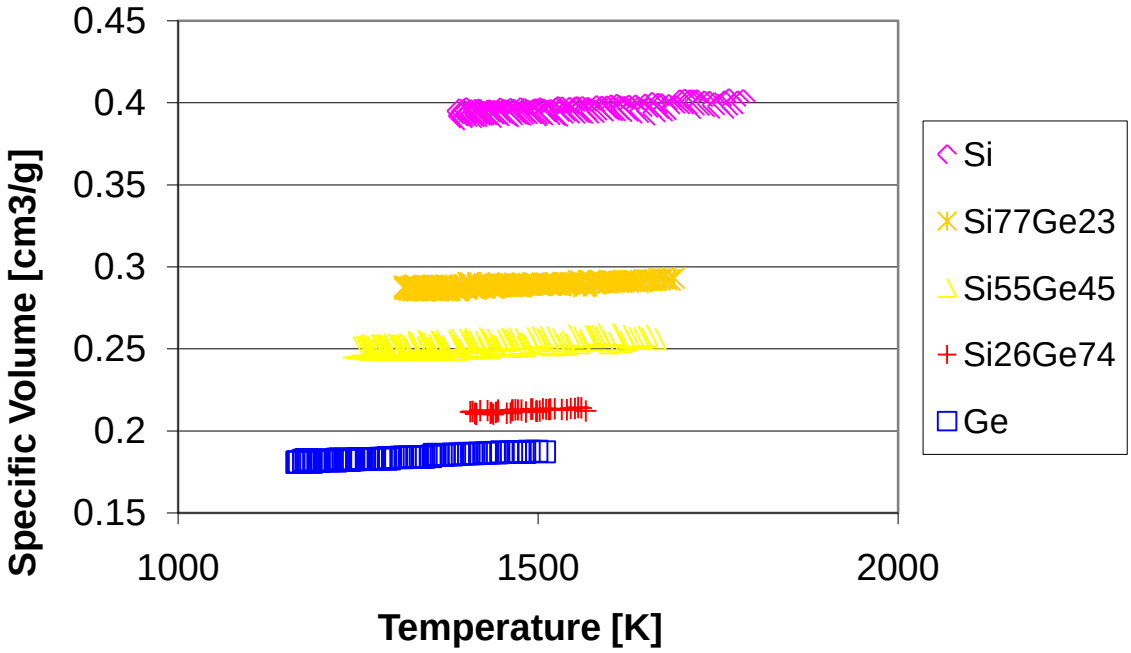

Figure 5.1: Specific volume of molten Si_xGe_{1-x} for x = 0, 0.26, 0.55, 0.77 and 1 around melting temperature.

Thermal expansion coefficients of volume at melting temperature are:

$$\beta = (\frac{1}{v})(\frac{dv}{dT})_{T=Tm} = b/(a + bT_M) \quad [K^{-1}]. \qquad (5.2)$$

Table 5.1 lists the results from parabolic flights [15], current measurements and some data of molten Si and Ge published before [7, 9]. We found that, for pure Si and Ge, the density and thermal expansion coefficient data all agree each other.

Table 5.1: Comparison with previous measurements on molten Si, Ge, and their alloys

Sample	Density at T_{liq} [g/cm^3]	T_{liq}[K]	β [$10^{-4}K^{-1}$]	Reference	Methods
Ge	5.49 ± 0.01	1211	1.09±0.01	Present work	ESL
Ge	5.67	1211	0.9656	Rhim [7]	ESL
Ge	5.57 ± 0.01	1211	1.06 ± 0.02	Chathoth [15]	Parabolic Flight
$Ge_{74}Si_{26}$	4.72±0.01	1433	0.802	Present	ESL
$Ge_{75}Si_{25}$	5.26±0.01	1423	0.73±0.01	Chathoth [15]	Parabolic Flight
$Ge_{45}Si_{55}$	3.91±0.01	1563	0.63±0.01	Present	ESL
$Ge_{50}Si_{50}$	5.87±0.01	1548	1.79±0.02	Chathoth [15]	Parabolic Flight
$Ge_{23}Si_{77}$	3.44±0.01	1623	0.52±0.01	Present	ESL
$Ge_{25}Si_{75}$	4.46±0.01	1623	3.06±0.02	Chathoth [15]	Parabolic Flight
Si	2.51 ± 0.01	1687	0.43±0.01	Present	ESL
Si	2.52±0.01	1687	1.37±0.02	Chathos[15]	Parabolic Flight
Si	2.583	1687	0.74	Zhou [9]	ESL

From the Equation 5.1, we can calculate the molar volume of liquid Si_xGe_{1-x} in a full composition range as a function of temperature.

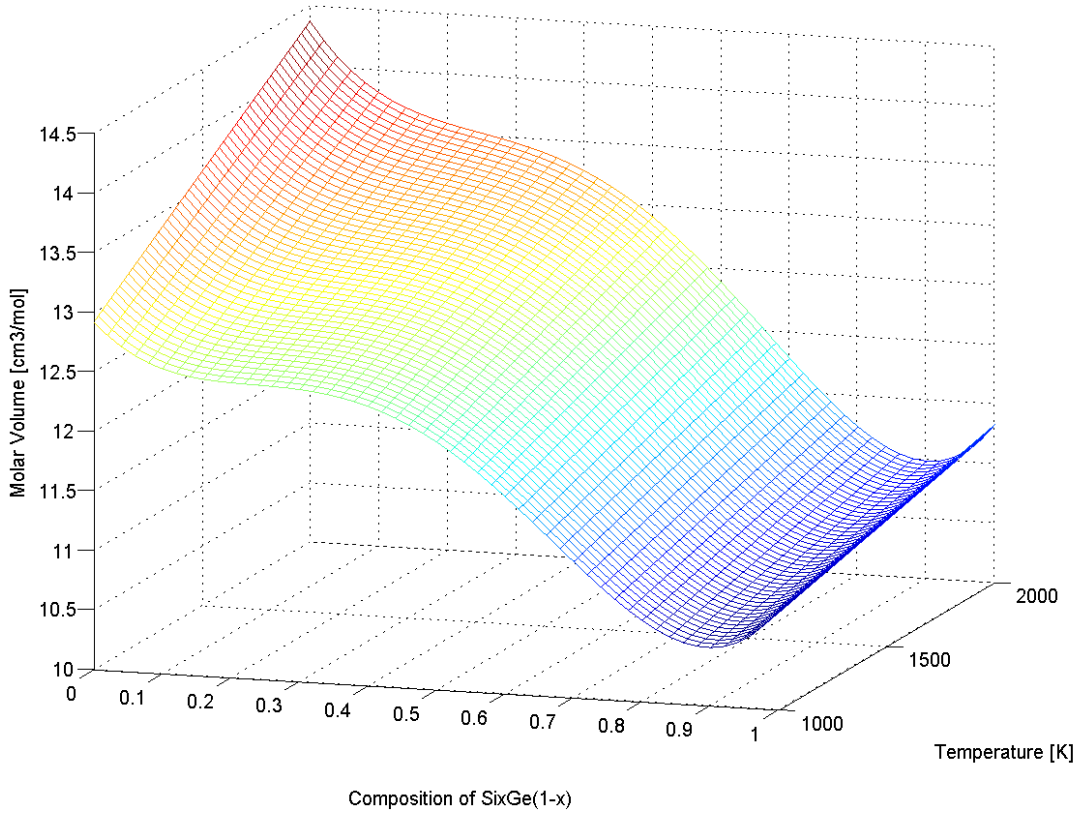

Figure 5.2. molar volume of liquid Si_xGe_{1-x} at temperature *T*, derived from the Equation 5.1

Figure 5.2 shows dependence of the molar volume of liquid Si_xGe_{1-x} changes on the temperature and composition. We noticed that molar volume of molten Si_xGe_{1-x} decreases with the addition of Si in a non-linear way and the thermal expansion coefficient is higher on the Ge rich side than the Si rich side.

molar excessive volume shows how a mixed solution deviates from an ideal solution and therefore gives an insight of the bonding structure of mixed liquid. It also helps the modeling in applying the mixing rules. The molar excessive volume of molten Si_xGe_{1-x} at temperature T can be calculated by $\Delta V_E = V - [xV_{Si} + (1-x)V_{Ge}]$, where V_{Si} and V_{Ge} are the molar volume of Si and Ge.

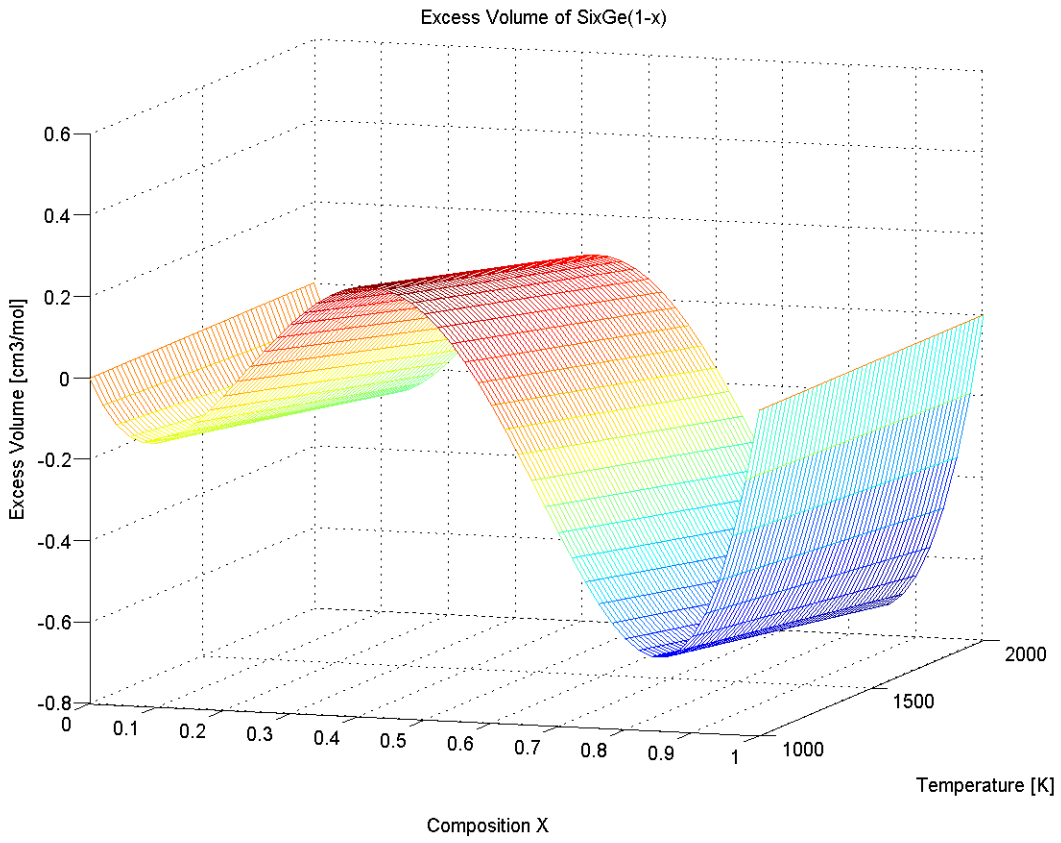

Figure 5.3: molar excessive volume of Si_xGe_{1-x}, calculated from equation Eq. (5.1)

Figure 5.3 shows a 3-dimensional molar excessive volume of Si_xGe_{1-x}. It shows that the bottom of this curve is located near $x \sim 0.85$.

Solid Ge-Si alloys form random diamond cubic over the entire composition range. Recent synchrotron X-ray diffraction measurements [18] and energy-dispersive X-ray diffraction measurements [16, 19] on molten Si, Ge, and $Si_{50}Ge_{50}$ showed that the coordination number (CN) to be about 6. This implies covalence bonding in their liquid state. Our results in Figure 5.3 show that adding up to 15% of Ge into Si can reduce the molar excess volume. This may suggest an increase in CN with more metallic bonding into the covalence bonding of Si for liquid Si_xGe_{1-x}, $0.7< x <1$. This should be verified by the synchrotron X-ray diffraction on a levitated molten sample.

Our specific volume results do not show any evidence of anomalous change in undercooled region of Si_xGe_{1-x} alloys.

5.4.2 Viscosity

Viscosities and surface tension of liquid Si_xGe_{1-x}, (where x=0, 0.25, 0.5, 0.75, and 1) samples were measured by the ESL. Figure 5.4 shows the viscosity of measured liquid Si_xGe_{1-x} alloys. The composition changes in this Figure is the result of the calibration we made due to evaporation of Ge We find that $Si_{52}Ge_{48}$ has a higher value of viscosity than the other alloys, which may indicate a good composition for glass-forming, according to the discussion in Chapter 6.

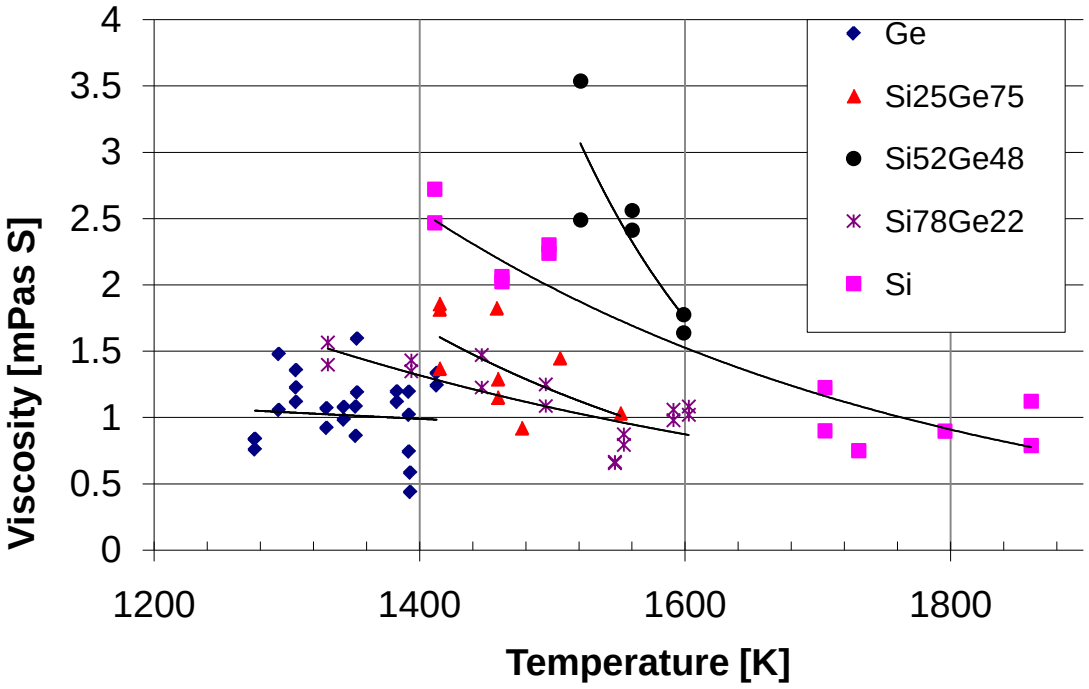

Figure 5.4: Viscosities of liquid Si_xGe_{1-x}, for x= 0, 0.25, 0.52, 0.78 and 1

Since this is the first time measuring the viscosity of mixed Si_xGe_{1-x} alloys, the only data we can compare with are the data of pure Si we reported before [9] and by Sasaki [20]. The results are shown in Figure 5.5. It shows that the results of present measurements agree well with the other measurements near the melting temperature of Si at 1687 K and we were able to reach a deeper undercooling of 276 degree than the previous reported data. The viscosity at deep undercooling region supports our previous statement that no anomalous increase of viscosity with decreasing temperature nears the melting temperature [9].

Figure 5.4 shows that the viscosities of Si_xGe_{1-x} increase with increasing x in the range0< x<0.5. They decrease with increasing x in the range 0.5<x<0.78, and increase again when

x approaches 1. These results suggest that atoms in liquid Si have stronger valence bonding. Adding a small amount of Ge (<30%) reduces its viscosity. This explanation also agrees with our conclusion from the specific volume measurements.

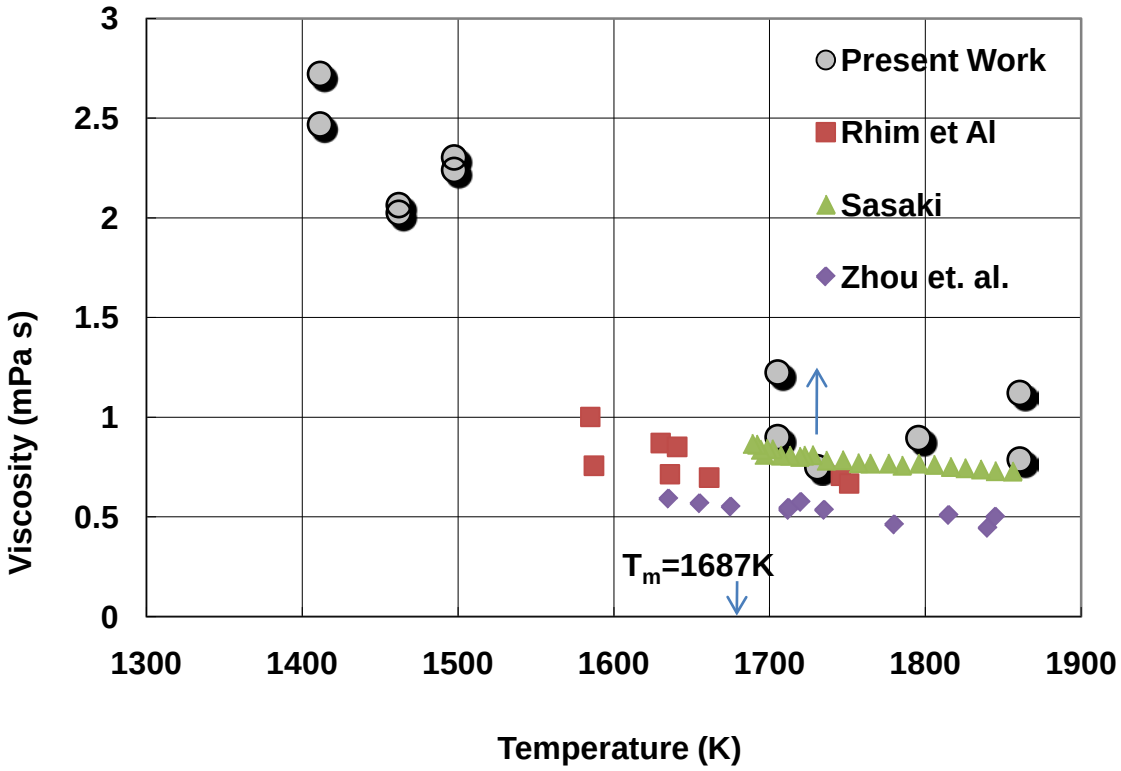

Figure 5.5: Comparison of presently measured viscosity of liquid Si with the literature values.

5.4.3 Surface tension

The surface tensions of liquid Si_xGe_{1-x} are shown in Figure 5.6. The measured surface tensions of molten Si by Zhou *et al.* using the ESL [9], and the data of Si_xGe_{1-x} by Chathoth *et al* .measured during the parabolic flights [15] are also plotted. In Chathoth's experiments, the temperatures associated with the surface tensions measurements were not specified so we are plotting their data with their liquidus temperatures. The measurements by ESL provide dependence of surface tension on the temperature, which are the first data on these mixed liquid alloys.

The surface tension measurements of molten Si in this report have extended a much deeper undercooling temperature region than the previous report by Zhou *et el*. Except for the Si that shows a positive temperature gradient of surface tension, the other four alloys show almost constant values over the temperature range investigated. The surface tension of a liquid should decrease with rising temperature because the interface between liquid and gas disappears as the critical temperature is reached. Positive temperature gradient for surface tension in some alloys may be due to the surface segregation of low surface tension elements with increasing undercooling. Figure 5.6 shows the surface tensions of molten Si with positive temperature gradient. It suggests that the predicted liquid-to-liquid phase transition below the melting temperature could be associated with a surface segregation [17]. The MD simulation suggests a surface segregation at composition of $Si_{80}Ge_{20}$ [20], but our results of surface tensions have not shown any evidence to support this because the surface tension of liquid $Si_{80}Ge_{20}$ remains as a constant in the temperature range that we studied with about 300 degree undercooling.

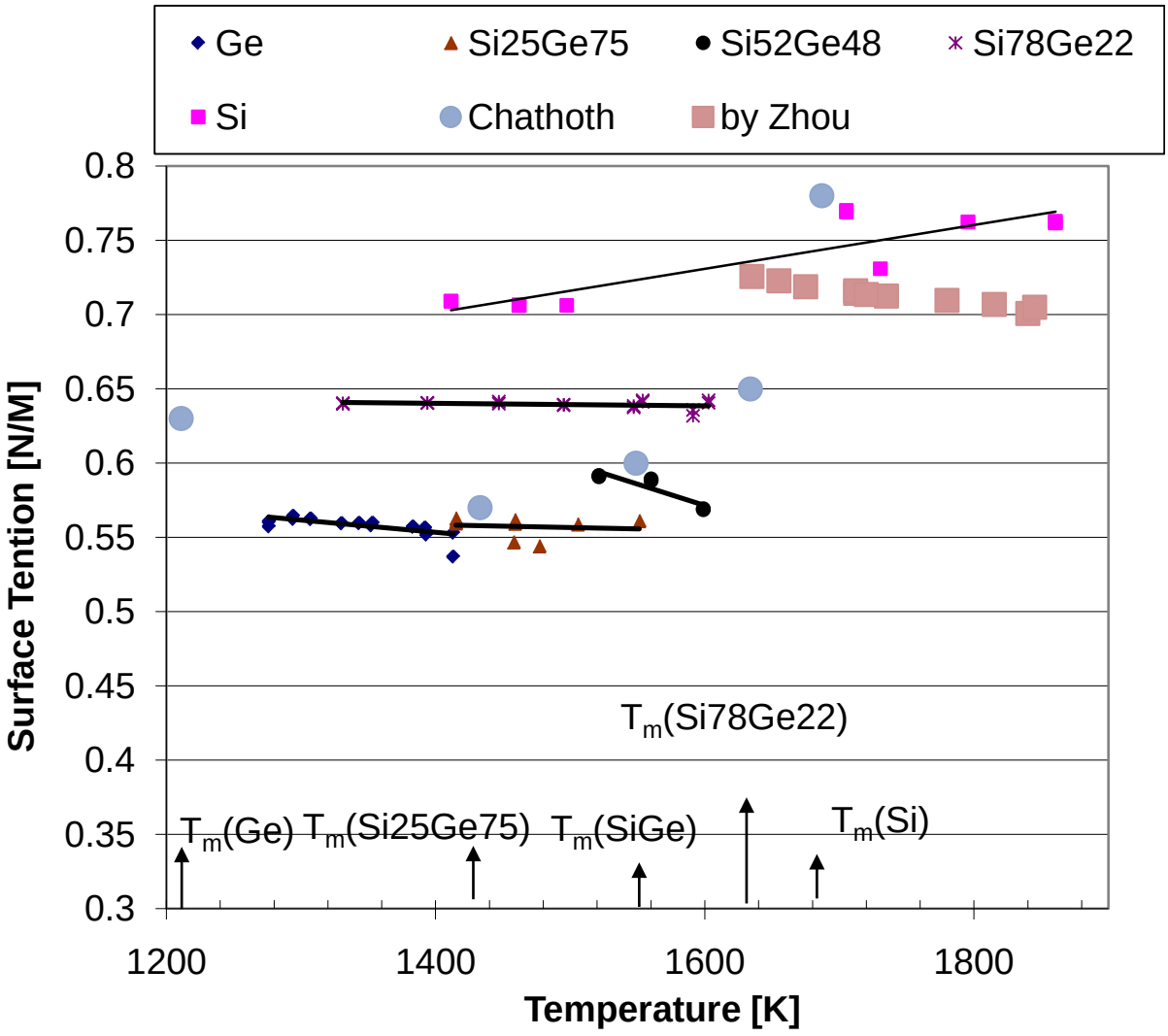

Figure 5.6: Surface Tension of molten Si_xGe_{1-x}, where x=0, 0.25, 0.52, 0.78, and 1

5.5 Conclusion

With the Electrostatic Levitator and non-contact measuring techniques we have successfully measured the specific volume, viscosity and surface tension of Si_xGe_{1-x} at x=0, 0.25, 0.5, 0.75 and 1 from above liquidus temperature to undercooled temperature region. By fitting data, we created a formula for specific volume and thermal expansion coefficient of liquid Si_xGe_{1-x}, showing their dependence on the temperature and the composition. The viscosity of Si with a 276 degree undercooling also confirmed our previous observation of no anomalous increase of viscosity with the temperature decrease at melting temperature.

The specific volume data of liquid Si does not support the prediction of a first order liquid-to-liquid phase at 1345 K, but our surface tension data of liquid Si suggest a surface segregation upon deep undercooling.

5.6 References

[1] Y. Asakuma, S. H. Hahn, Y. Sakai, T. Tsukada, M. Hozawa, T. Matsumoto, H. Fujii, K. Nogi, and N. Imaishi, Metallurgical and Materials Transactions B-Process Metallurgy and Materials Processing Science **31**, 327 (2000).

[2] Y. Asakuma, T. Hirata, T. Tsukada, M. Hozawa, K. Nogi, and N. Imaishi, Journal of Chemical Engineering of Japan **33**, 861 (2000).

[3] H. Fujii, T. Matsumoto, S. Izutani, S. Kiguchi, and K. Nogi, Acta Materialia **54**, 1221 (2006).

[4] H. Kawamura, H. Fukuyama, M. Watanabe, and T. Hibiya, Meas. Sci. Technol. **16**, 386 (2005).

[5] F. Millot, V. Sarou-Kanian, J. C. Rifflet, and B. Vinet, Materials Science And Engineering A-Structural Materials Properties Microstructure And Processing **495**, 8 (2008)

[6] K. C. Mills and Y. C. Su, International Materials Reviews **51**, 329 (2006).

[7] W. K. Rhim and T. Ishikawa, (Kluwer Academic/Plenum Publ, 2000), p. 429.

[8] Y. S. Sung, H. Takeya, K. Hirata, and K. Togano, Applied Physics Letter **83**, 1122 (2003).

[9] Z. H. Zhou, S. Mukherjee, and W. K. Rhim, Journal of Crystal Growth **257**, 350 (2003).

[10] S. Kimura and K. Terashima Journal of Crystal Growth **180**, P. 323.(1997)

[11] M. Inui, T. Matsusaka, D. Ishikawa, Y. Sakaguchi, X. G. Hong, M. H. Kazi, and K. Tamura, (Munksgaard Int Publ Ltd, 2001), p. 767

[12] T. Aoyama, Y. Takamura, and K. Kuribayashi, Japanese Journal of Applied Physics Part 2-Letters **37**, L687 (1998).

[13] A. Croll, N. Salk, F. R. Szofran, S. D. Cobb, and M. P. Volz, Journal of Crystal Growth **242**, 45 (2002).

[14] P. Dold, A. Barz, S. Recha, K. Pressel, M. Franz, and K. W. Benz, Journal of Crystal Growth **192**, 125 (1998).

[15] S. M. Chathoth, B. Damaschke, K. Samwer, and S. Schneider, Applied Physics Letter **93**, 3 (2008).

[16] Y. Naito, M. Inui, T. Anai, and K. Tamura, (Elsevier Science Bv, 2007), p. 3376.

[17] C. A. Angell and S. S. Borick, Journal of Physics-Condensed Matter **11**, 8163 (1999).

[18] S. Krishnan, L. Hennet, T. Key, B. Glorieux, M. L. Saboungi, and D. L. Price, Elsevier Science Bv, 2007), p. 2975

[19] H. Kimura, *et al*., Applied Physics Letter **78**, 604 (2001).

[20] H. Sasaki, E. Tokizaki, X. M. Huang, K. Terashima, and S. Kimura, Japanese Journal of Applied Physics Part 1-Regular Papers Short Notes & Review Papers **34**, 3432 (1995)

. [21] W. B. Yu and D. Stroud, Physical Review B **56**, 12243 (1997).

6 Thermophysical Properties of BMG Alloys in Undercooled Liquid Region

6.1 Abstract

The thermophysical properties of some glass-forming metallic liquids studied by ESL show that both glass-forming ability and properties of the solid BMGs are related to the liquid viscosity in the undercooled temperature range between T_g and T_l. Our study revealed that GFA is closely related to the viscosity near T_l. whereas the ductility and toughness of the glass can be correlated with the viscosity changes with temperature near T_g. A best fit of the critical cooling rate for glass-formation can be expressed by $R_c = Exp[13.7 - 2.09 * \ln(\eta(T_l))]$ [K/s] with the viscosity in [mPas s]. Liquid volume changes of Vit1 and LM7observed above T_l. suggest a liquid-to-liquid phase transition occurs in the alloys above their liquidus temperatures. This may explain both the hysteresis effects in their viscosities and also the threshold temperature effect observed.

6.2 Introduction

One of the most promising developments in international metals community in recent years has been the development of bulk metallic glasses (BMGs). Glass is a solid without long range order. Glasses are formed when the liquids solidify without crystallization. Metallic glasses offer attractive properties, combining some of the desirable properties of conventional crystalline metals with the formability of polymer glasses and conventional oxide glasses. The concept of metallic glasses was first introduced by Turnbull *et al.* [1] in the 1950s. He argued that pure metallic melts can achieve deep undercooling or even become amorphous if the cooling rates are high enough. In 1960, Klement *et al.* [2]

reported the first non-crystalline glassy structure in a solidified Au-Si alloy produced by rapid quenching from melt at cooling rate of 10^6 K/s. By adding more elements into the melt, the alloy melting temperature can be lowered and the glass-forming ability (GFA) can be improved. By adding Ge into Au-Si, for example, Chen [3] and his co-workers lowered the liquidus temperature by 10 K and vitrified an Au-Si-Ge melt at a cooling rate of 10^3 K/s. In the early 1990s, Inoue and co-workers discovered new ternary alloys of Zr-X-Y (X=Al, Y= Ni, Cu, Co) that required a quenching rate of 10^2 K/s to produce a glass phase [4]. In 1993, Peker and Johnson reported a highly processable metallic glass $Zr_{41.2}Ti_{13.8}Ni_{10}Cu_{12.5}Be_{22.5}$ (Vit1) which enabled a critical cooling rate of 1 K/s [5]. These alloys mark the advent of the second-generation BMGs.

BMGs tend to be strong, hard, and wear-resistant, yet can be molded on a fine scale, which provides an opportunity for industrial applications such as molding golf clubs and cell phone cases [6--9], creating amorphous foam [10--13], doing micro-replication [14, 15], blow-molding [16], and forming amorphous composites [17--19] etc. The importance of better understanding the thermodynamic and kinetic properties of BMGs in undercooled liquid region (UCLR) has been realized and many studies have been published.

At Caltech we have used the ESL to investigate the thermophysical properties of BMGs in the UCLR as described in Chapter 1. The non-contact diagnostic techniques for measuring those thermophysical properties in the UCLR were described in Chapter 3. Two major subjects are studied on BMGs in this thesis:

a) How to improve the GFA

GFA is one of the major subjects of BMGs [20--24]. It has been reported that GFA is associated with the volume changes at melting temperature and also with the viscosity of the liquid at nose temperature of the time-temperature-transformation (TTT) curve for crystallization [22]. The threshold temperature, which is the overheating temperature above the liquidus for which subsequent undercooling is enabled, has also been found to influence the GFA [24].

b) How to improve the ductility of BMGs

BMGs have most of the desirable qualities of metals except ductility and toughness. This often prevents the application of BMGs in broader fields. Many researchers have been focusing on improving the ductility and toughness of BMGs, or designing new composites [18, 25, 26].

In this chapter, the GFA and ductility of BMGs are discussed along with their relationship to their thermophysical properties in the UCLR. A guiding principle for better GFA based on our experimental measurements is provided. We also offer an explanation on some unsolved questions in Vit1 and LM7 by providing evidence of a liquid-to-liquid phase change taking place above the liquidus temperatures of the alloys.

6.3 Influence of Thermophysical Properties of BMGs in UCLR on GFA and Ductility

6.3.1 Glass-forming ability

GFA is important for exploring and developing new BMGs. GFA is associated with the critical size that a BMG material can be cast or equivalently with the lowest cooling rate of the liquid (R_c) necessary to produce an amorphous solid free of crystals during

solidification. The bigger in critical size, the better the GFA is. The smaller R_c, the higher the GFA of a system should be. Figure 6.1 illustrates the concept of R_c using a TTT curve.

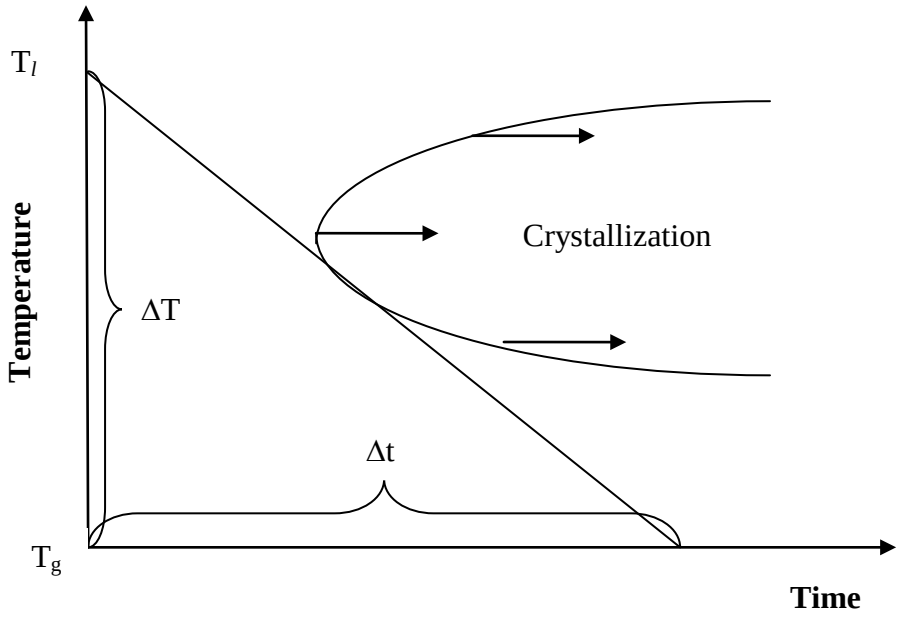

Figure 6.1: Illustration of Critical Cooling Rate on a TTT curve. The critical cooling rate is $\boldsymbol{R_c \sim \frac{\Delta T}{\Delta t}}$

A time-dependent volume fraction of crystalline phase X is given based on the non-isothermal crystallization kinetics [27, 28]:

$$X(T) = \frac{4\pi}{3R^4} \int_{T_l}^{T_g} I(T') [\int_{T'}^{T_g} U(T'') dT'']^3 dT''. \qquad (6.1)$$

here I and U are the steady-state crystal nucleation frequency and the crystal growth rate, respectively. If one selects $X < 10^{-6}$ as a criterion for glass-formation, then the critical cooling rate R_c can be derived from Eq. (6.1) as:

$$R_c^4 = \frac{4\pi}{3\times10^{-6}} \int_{T_l}^{T_g} I(T')[\int_{T'}^{T_g} U(T'')dT'']^3 dT'. \quad (6.2)$$

According to the common crystallization theory, the nucleation frequency and crystal growth rate can be expressed by the following equations [29, 30]

$$I = AD_{eff} \exp(-\frac{\Delta G^*}{k_B T}), \quad (6.3)$$

where, A is a constant, $k_B$is the Boltzmann's constant, D_{eff} is the effective diffusivity which can be estimated by the Stokes- Einstein equation, $D_{eff} = k_B T/(3\pi\eta a)$, where η is the dynamic viscosity of the liquid, and $\Delta G^*$is the activation barrier for nucleation,

$$\Delta G^* = \frac{16\pi\Delta S_f(\alpha T)^3}{3N_A(T_l - T)^2}. \quad (6.4)$$

The growth rate is

$$U = \frac{D_{eff}}{a}\left[1 - \exp\left(-\frac{(T_l - T)\Delta S_f}{N_A k_B T}\right)\right], \quad (6.5)$$

where ΔS_f, α, N_A, and a are molar fusion entropy, a structure factor, Avogadro's number, and inter-atomic spacing of the alloy, respectively.

The nucleation rate and the growth rate vs. temperature are illustrated in Figure 6.2 for Vit1 from Muhkerjee *et al*. [20]. He found that the nucleation rate and growth rate at the "nose" temperature T_N in its TTT curve plays the most important role in crystallization. He claimed that $\ln(R_c) \propto \frac{1}{\eta(T_N)}$, where $\eta(T_N)$ is the viscosity of the liquid at nose temperature.

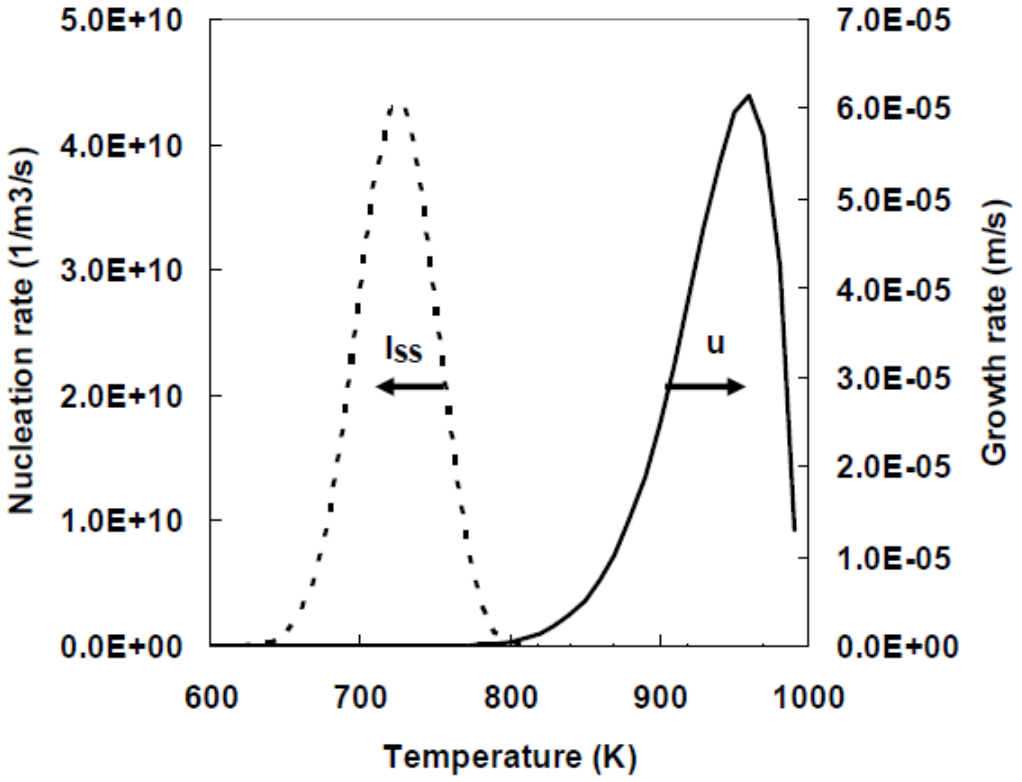

Figure 6.2: Illustration of growth rate of Vit2

From Equation 6.2 we can approximate the critical cooling rate by

$$R_c \propto \left(I(T_\gamma)U^3(T_\gamma)\right)^{1/4} \propto \frac{F(T_\gamma)}{\eta(T_\gamma)}, \tag{6.6}$$

where $F(T)$ represents the thermodynamic properties of both liquid and crystal and T_γ is a temperature to be determined between T_l and T_x (the liquidus and crystallization onset temperature respectively),

$$T_\gamma = T_x + \gamma(T_l - T_x), \tag{6.7}$$

where γ is a constant to be determined. The viscosity at T_γ can be estimated by extrapolating the viscosity measured near liquidus temperature.

6.3.2 Ductility of amorphous metals

The ductility of amorphous metals has been studied by many researchers. The fragility of a liquid has been correlated with the ductility of the solid glass [31--33]. Schroers and Johnson have shown that the ductile behavior of BMGs is closely related to their Poisson's ratio [32] and Novikov *et al.* have shown a correlation between Poisson's ratio and fragility index *m* [43]. Angell defined liquid fragility *m* as the gradient of viscosity curve at glass transition temperature on a reduced temperature scale [34]:

$$m = \left(\frac{d \log_{10} \eta}{d\left(\frac{T_g}{T}\right)} \right)_{T=T_g} . \qquad (6.8)$$

The rheology of glass-forming metallic liquid has been described in two types of phenomenological theories: free volume theories and shear transformation zone theories [35--39]. The experimental measurement of viscosity near melting temperature is limited by the chemical reaction between the sample and the container walls. So far, most viscosity data for BMG liquids near the liquidus temperature were obtained by ESL. ESL has an advantage in the stability of sample position compared with EML in studying viscosity of BMG liquids in the UCLR.

6.4 Viscosities of Liquid BMG Alloys in the UCLR

6.4.1 Measurements of viscosities

With the technique described in Chapter 3, the viscosities of several BMGs at the UCLR have been measured by the ESL at Caltech as shown in Figure 6.3 [40--41]. The critical cooling rate of these glass-forming alloys ranges from 500 K/s to 1 K/s.

The viscosity at the high end of UCLR is observed to follow an Arrhenius relation, which can be described by

$$\ln \eta = A + \frac{B}{T} \qquad (6.9)$$

where *A* and *B* are constants. Figure 6.4 shows *log* η *vs. (1/T)* and we notice that the linear fit of *Log(*η*(1/T))* data all points to an η_0 of the order of 10^{-3} [mPas s] as *(1/T)* approaches 0. This is close to the lower limit of viscosity at high temperature, estimated by Eyring's concept of rate theory [42] $\eta_0 = h/v$ (~4×10^{-2} mPas s for Vit1), where *h* is the Plank constant and *v* is the average atomic volume.

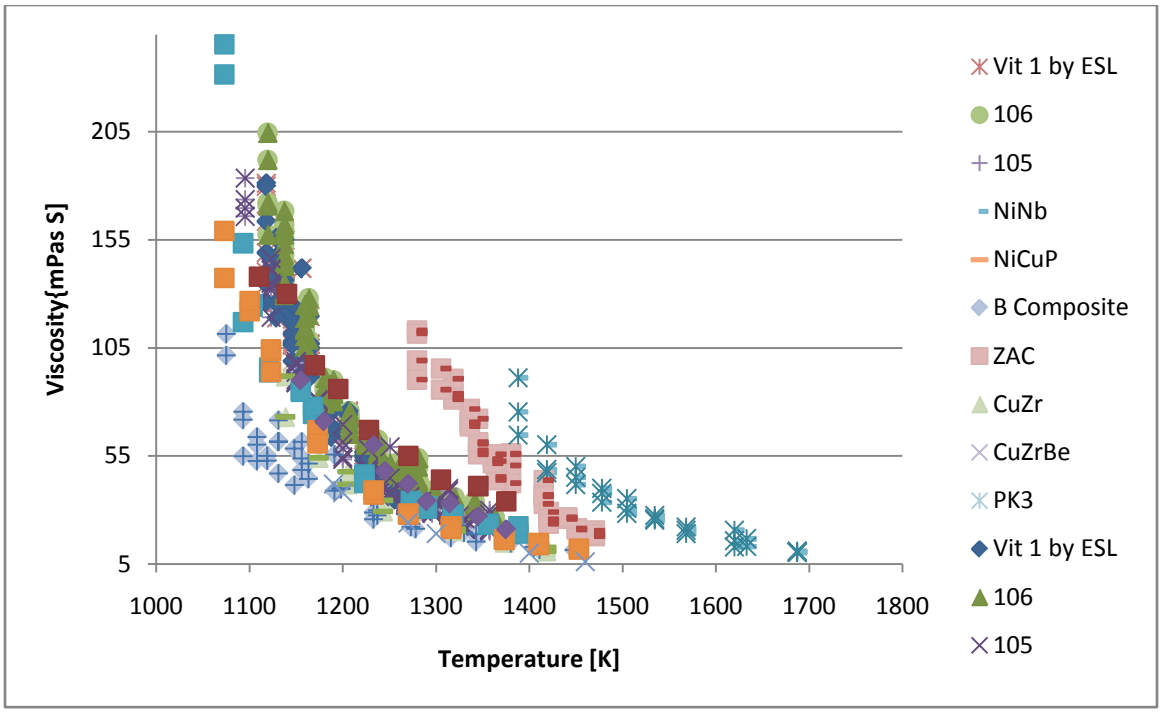

Figure 6.3: Viscosity of some BMGs measured by ESL at Caltech

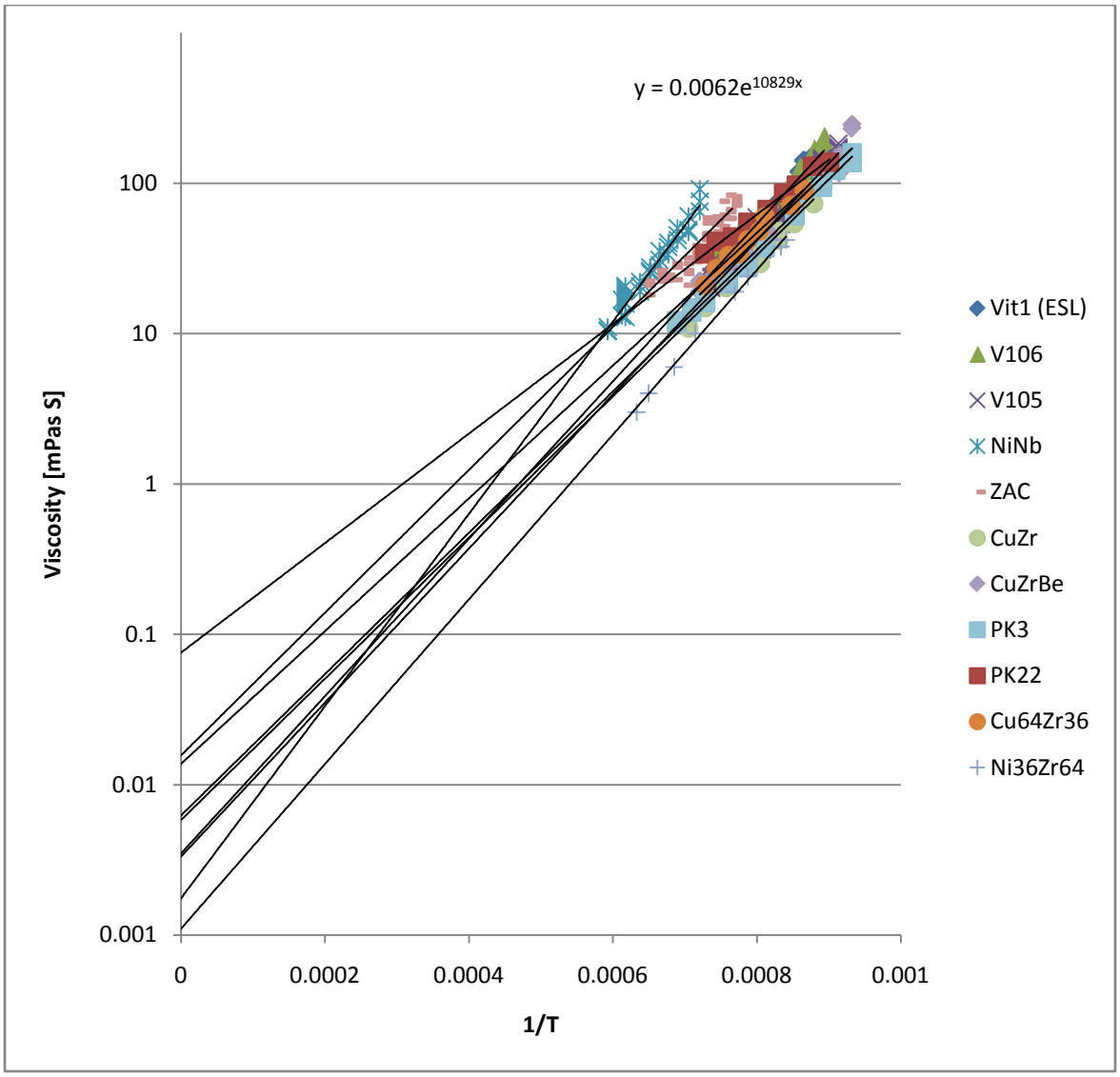

Figure 6.4: Viscosity of some BMGs versus *1/T*. The linear fit of *ln(η)* point to a same high temperature viscosity limit in the order of 10^{-2} [mPas s]

From Equation 6.8 we can estimate the viscosity at shallow undercooling temperature *T*:

$$\frac{\ln(\eta(T))-\ln(\eta_0)}{\ln(\eta(T_l))-\ln(\eta_0)} = \frac{\frac{1}{T}}{\frac{1}{T_l}} = \frac{T_l}{T}, \qquad (6.10)$$

This can be simplified by,

$$\frac{\eta(T)}{\eta_0} = \left(\frac{\eta(T_l)}{\eta_0}\right)^{\frac{T_l}{T}}. \tag{6.11}$$

6.4.2 Comparison of critical cooling rates with viscosities

With Equation 6.6, 6.7 and 6.11, we can estimate the critical cooling rate to be

$$R_c \propto \left(\frac{\eta(T_l)}{\eta_0}\right)^{-\frac{T_l}{T_x+\gamma(T_l-T_x)}},$$

or

$$\ln(R_c) = A - \frac{T_l}{T_x+\gamma(T_l-T_x)}\ln\left(\frac{\eta(T_l)}{\eta_0}\right). \tag{6.12}$$

From the data shown in Table 6.1 we have calculated R_c according Equation (6.12). Selecting $\eta_0 = 8 \times 10^{-3}$ [mPas S], Figure 6.5 shows $\ln(R_c)$ versus $\frac{T_l}{T_x+\gamma(T_l-T_x)}\ln\left(\frac{\eta(T_l)}{\eta_0}\right)$ for γ=0.05, 0.1, 0.15, 0.4, and 1.

Table 6.1: The critical cooling rates, liquidus temperature, onset crystallization temperature, and viscosity at the liquidus temperature for BMG forming liquids studied

Material	R_c [K/S]	T_l [K]	T_x [K]	$\eta(T_l)$ [mPas s]
$Zr_{42.63}Ti_{12.37}Cu_{11.25}Ni_{10}Be_{23.75}$	1.8	993	712	600 [1]
Zr52.5Cu17.9Ni14.6Al10Ti5	7.75	1115	742	200
Zr57Cu15.4Ni12.6Al10Nb5	9.6	1090	727	180
$Ni_{60}Nb_{40}$	132	1448	924	45
$Cu_{50}Zr_{50}$	269	1200	717	78
$Zr_{55}Al_{22.5}Co_{22.5}$	97	1323	808	100

[1] There are two different value of viscosity for Vit1 at liquidus temperature, which will be discussed in 6.5

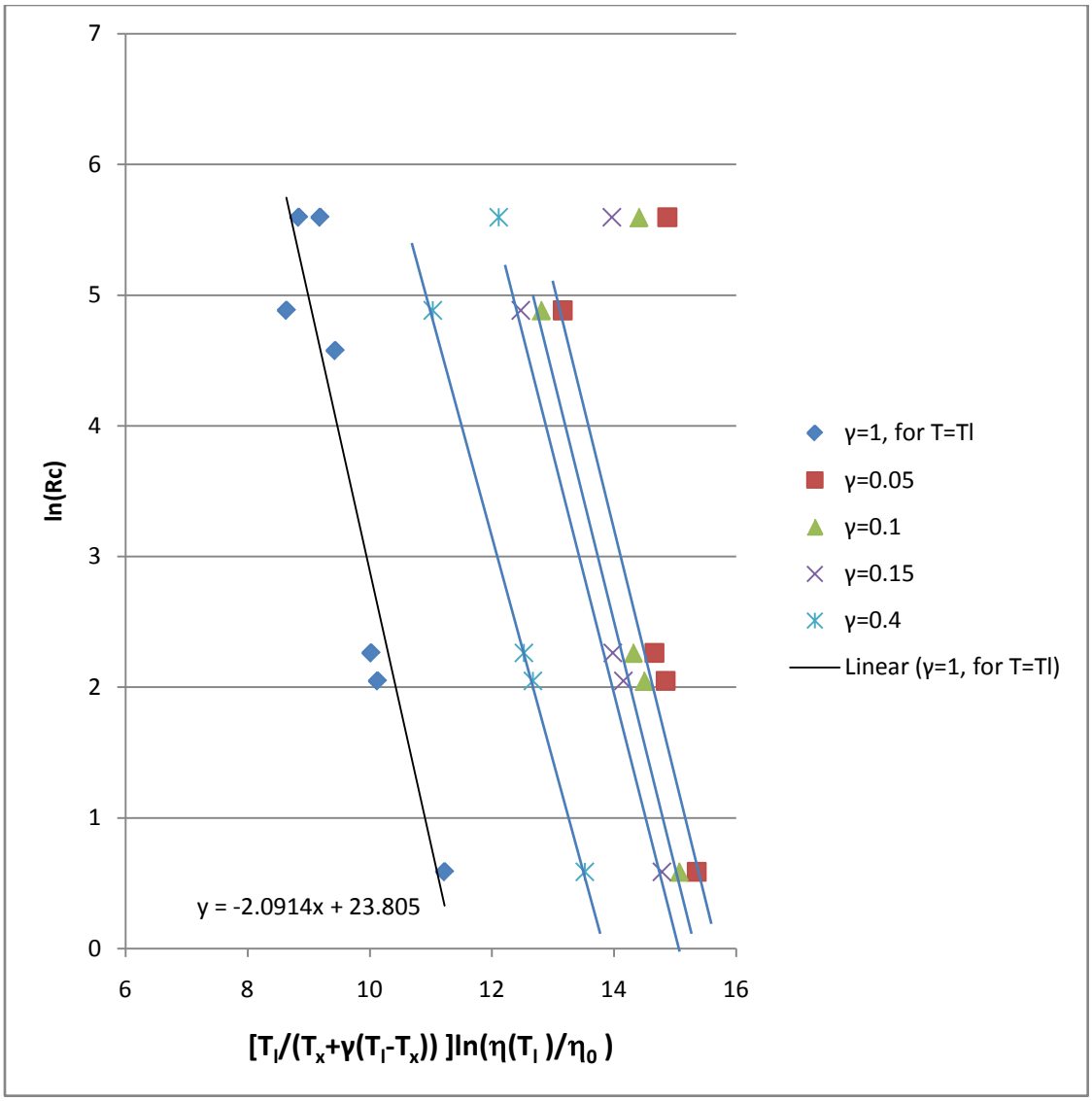

Figure 6.5: $\ln(R_c)$ versus $\frac{T_l}{T_x+\gamma(T_l-T_x)}\ln(\frac{\eta(T_l)}{\eta_0})$, selecting $\eta_0 = 8\times10^{-3}$ [mPas s], for γ=0.05, 0.1, 0.15, 0.4, and 1

From Figure 6.5, we found that γ=0.4 is the best linear fit. For γ=1 (i.e. $T_\gamma = T_l$), the best fit between the viscosity at liquidus temperature and the critical cooling rate of the alloy can be expressed as:

$$\ln(R_c) = 13.7 - 2.09 * \ln(\eta(T_l)). \quad (6.13)$$

Equation 6.13 provides a useful empirical relationship between the critical cooling rate [K/s] and the viscosity [mPas s] at liquidus temperature.

Compared with other criterions for GFA such as $T_{rg}(=T_g/T_l)$, ΔT_x $(=T_x - T_g)$, $\Delta T_{rg}(=(T_x - T_g)/(T_l - T_g))$, $\delta(=T_x/(T_l - T_g))$, $\gamma(=T_x/(T_g + T_l))$, $\gamma_m(=(2T_x - T_g)/T_l)$, $\phi(=T_{rg}(\Delta T_x/T_g)^{0.143})$, $\alpha(=T_x/T_l)$, $\beta(=T_x/T_g + T_g/T_l)$, $\beta(=T_x \times T_g/(T_l - T_x)^2)$ and $\varsigma(=T_g/T_l + \Delta T_x/T_x)$, as summarized by Long *et al.* [43], Equation (6.13) separates the kinetic parameter, the viscosity, and the thermodynamics parameters. While the kinetic properties (e.g. viscosity) of a liquid determine whether it is strong or fragile, the thermodynamics properties determine the liquidus temperature T_l. The lower the T_l, the higher the viscosity at liquidus temperature will be, and, therefore, the better GFA.

For a BMG, $R_c < 10^3$, equation 6.13 shows that the viscosity at liquidus temperature should be higher than ~26 [mPas s]. Equation 6.13 is plotted in Figure 6.6 which shows how the critical cooling rate is associated with the viscosity at liquidus temperature.

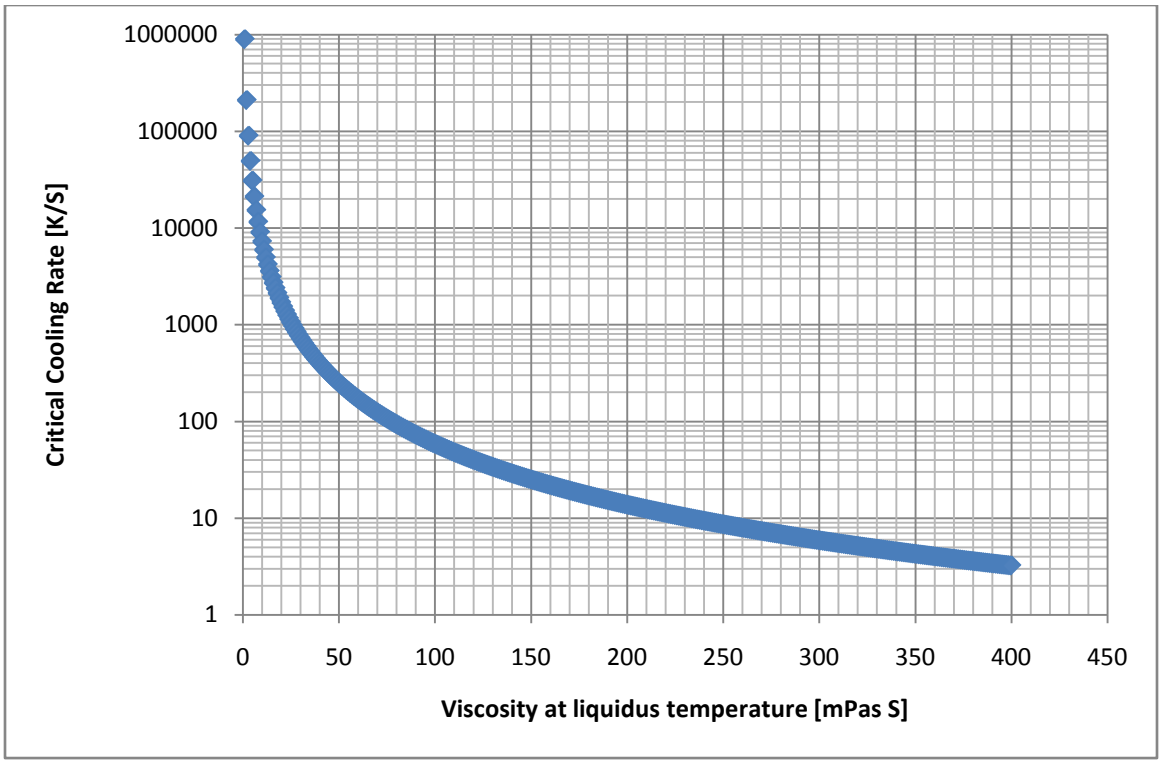

Figure 6.6: Plot of Eq. (6.13), which shows how the viscosity at liquidus temperature influences the critical cooling rate

More fragile liquids tend to freeze to glass with greater toughness and ductility, but a fragile liquid usually has a low viscosity at high temperature. Finding out the balance point of good GFA and fragility can be utilized to design novel BMGs. Fragility is related to the kinetic property of the liquid and the GFA is determined by both kinetic and thermodynamic properties of the liquid leading to the viscosity at liquidus temperature. From the discussion above we can conclude that the best glass-forming metallic alloys are formed from strong liquids with low liquidus temperatures. Ductile bulk metallic glasses are formed from fragile liquids which have both low values in viscosity and

liquidus temperature. Ductile bulk metallic glasses with high GFA are difficult to find from liquids with high liquidus temperatures.

6.5 Structure Changes in Vit 1 and LM7 in the UCLR

As we discussed above, the viscosity of a undercooled liquid plays an important role in the glass-forming ability. A recent measurement of the viscosity of Vit1 showed that the initial sample history prior to experimentation can affect the resulting viscosity measured above the liquidus [44]. As illustrated in Figure 6.7, Busch *et al.* found that molten Vit1 is kinetically strong when heated from low temperature to above the liquidus temperature at 1026 K. The viscosity dropped drastically to lower values upon heating to above 1225 K. It remains in such a “fragile” state until deeply cooled below liquidus temperature. Busch explained this phenomenon in terms of a polymorphous phase transition in the liquid.

This hysteresis in the viscosity curves of Vit1 was not found in the measurements by ESL because the upper limit of viscosity measured by ESL is ~250 [mPas s]. For higher viscosity, there is no oscillation. However, measurements on a similar BMG, LM7, show evidence of the hysteresis in viscosity above liquidus temperature. Figure 6.8 shows the viscosity of LM7 as measured by ESL at Caltech

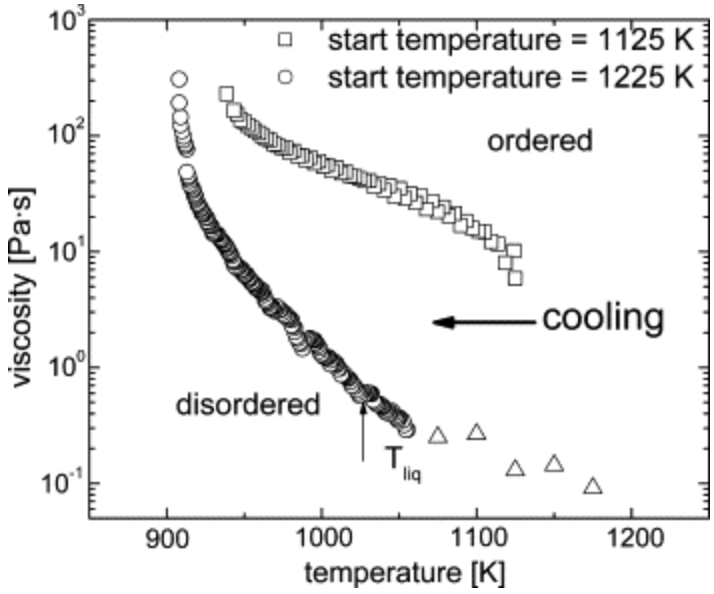

Figure 6.7: Viscosity versus temperature for continuous cooling with an average cooling rate of 2 K s^{-1} using a constant clockwise shear rate. When cooling from 1125 K (□), the viscosity stays about two orders of magnitude higher than when cooled from 1225 K (○). For the latter run, the data above 1045 K are not shown since the sensitivity of the torque sensor does not allow for accurate data. Data in this region (△) are represented by isothermal viscosity measurements. [41]

As described in Chapter 3, the sample was first heated to above 1500 K and then cooled to various temperatures. An AC voltage applied at resonance frequency of the drop generates an oscillation. The viscosity is calculated according to the decay of the oscillation amplitude. The viscosity increased drastically when the sample was cooled below ~1233 K. The sample remained as such a strong viscous liquid until heating is applied and temperature reaches above ~1320 K. At ~1320 K, the viscosity dropped back to its original value for the fragile liquid. These measurements are well above the liquidus temperature at 1033 K of the alloy and the results cannot be attributed to crystallization. We therefore suggest that the liquid undergoes some sort of phase transition which exhibits hysteresis. Whether it is only a kinetic change or thermodynamic phase change determine the type of the phase transition involved.

The DSC measurements on LM7 by Kim in Figure 6.9 suggest a small heat flow at *T* ~950 ℃ (or 1223 K), which seems to be the melting of some crystalline phase, but it is hard to understand how such a small amount of crystalline phase could create such dramatic changes in viscosity.

To further investigate whether there is a structure change in the liquid, the volume of molten liquids of Vit 1 and Lm7 were measured as shown in Figure 6.10 and Figure 6.11.

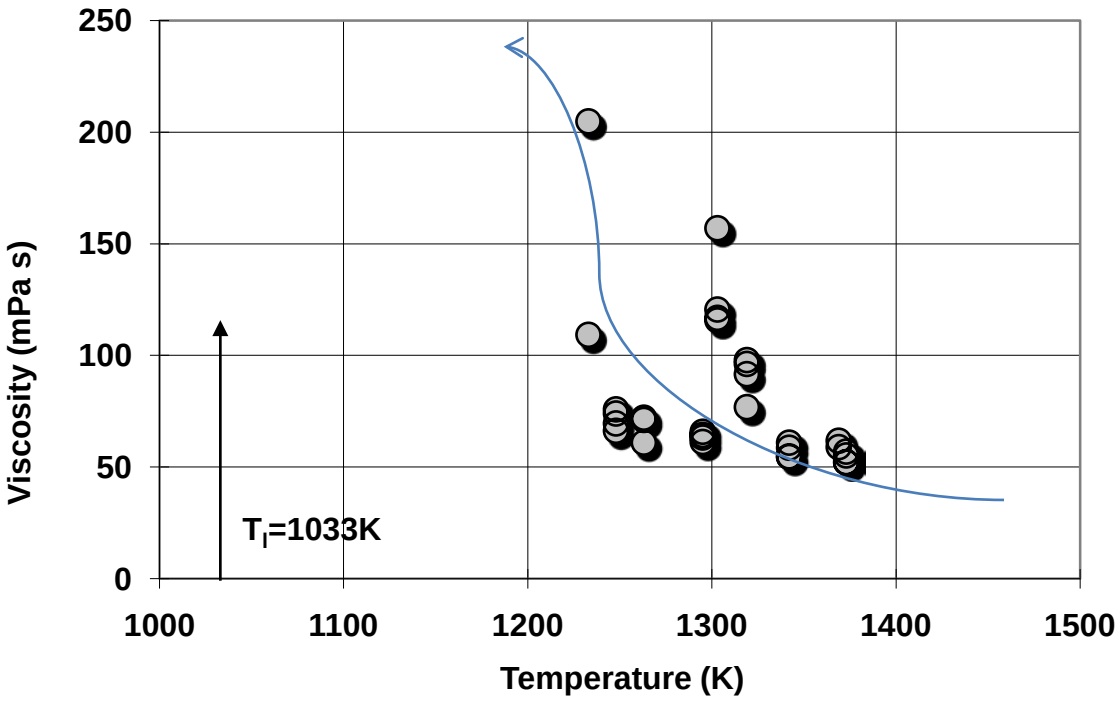

Figure 6.8: Viscosity of LM7. Sample was cooled from molten at 1500 K, and showed a dramatic increase in viscosity when cooled below 1223 K. Upon heating from 1100 K, the viscosity dropped back to its original curve at 1320 K.

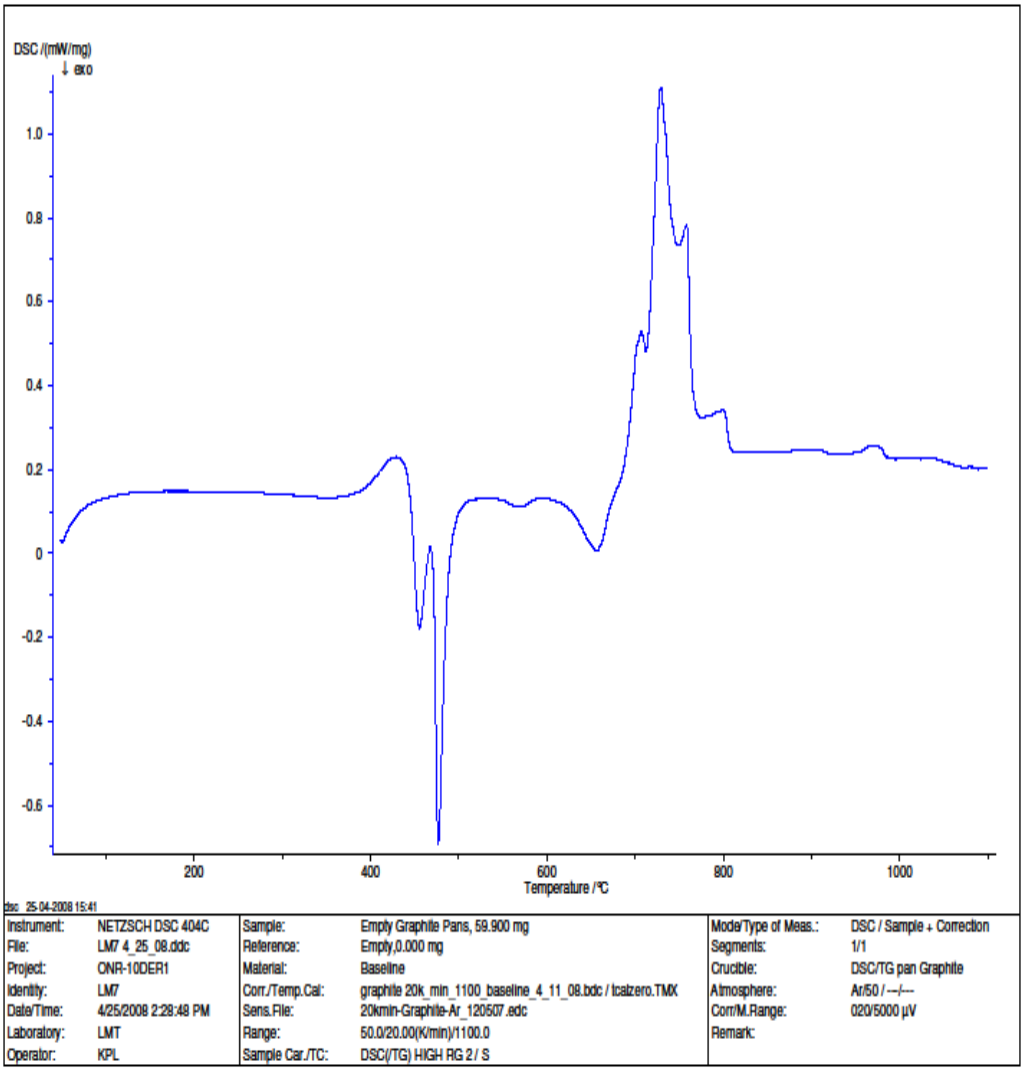

Figure 6.9: DSC measurement of LM7, which shows a small change at 950 ℃.

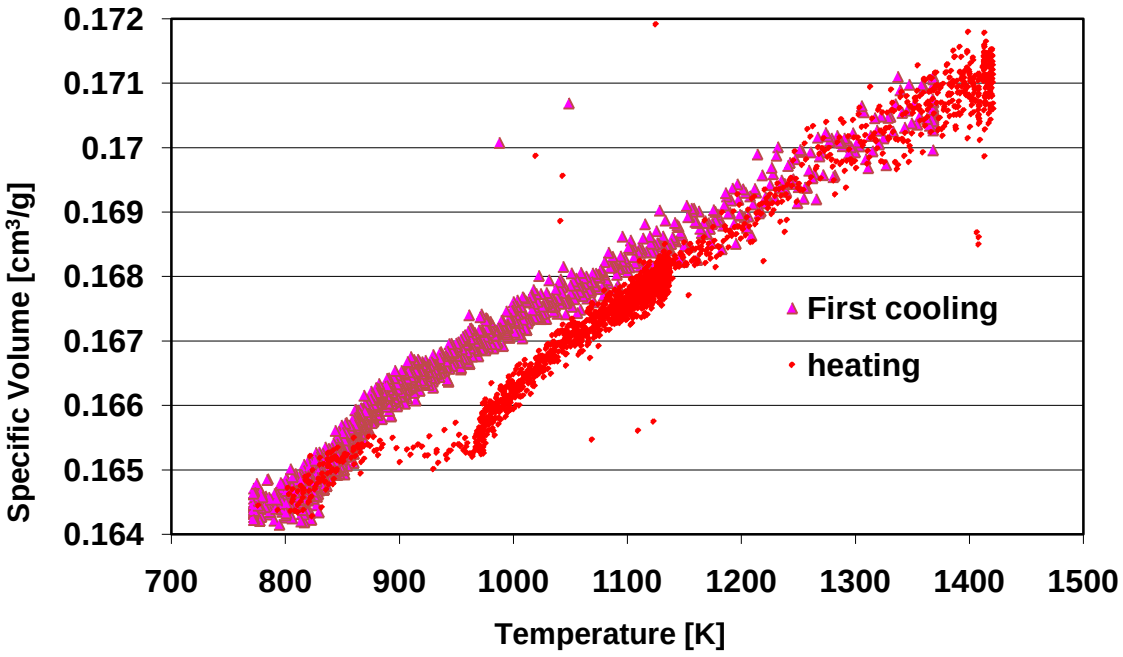

Figure 6.10: Specific volume of Vit1 upon cooling and heating. The volume was cooled from 1400 K and shows a sudden decrease below 870 K. Upon heating from 800 K, the sample partially crystallized and the temperature jumped to the solidus temperature. The volume in heating is smaller than in cooling until a threshold temperature 1250 K is reached.

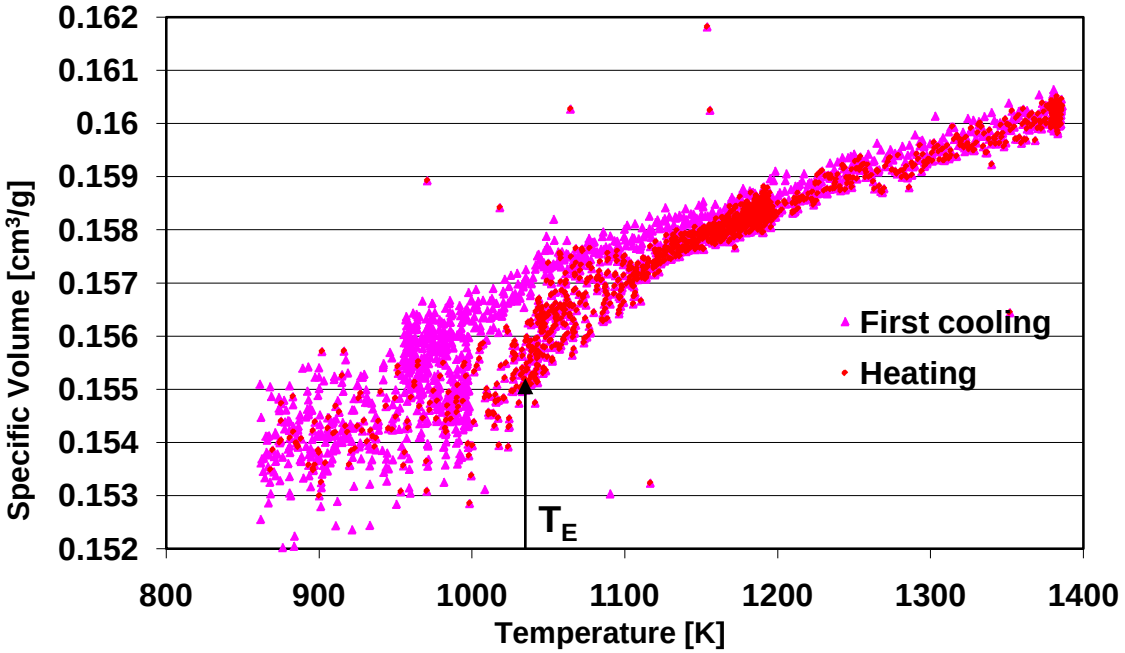

Figure 6.11: Specific volume of LM7 in cooling and heating. The volume at heating is smaller than in cooling until a threshold temperature of 1250 K is reached.

Both Figure 6.10 and Figure 6.11 show that the volume of the liquid on heating is lower than in cooling until a threshold temperature reached, which is about 1250 K for both Vit1 and LM7. The liquids with lower volume also show higher viscosities according to our concurrent viscosity measurements.

An earlier study on Vit1 by ESL showed that there is a threshold temperature for Vit1 at 1250--1300 K [45]. When the sample was preheated above 1300 K, the crystallization time was ~130 second when sample was isothermally annealed at 830 K, whereas for preheating less than 1250 K, the crystallization time at 830 K was only ~30 second. Lin

et al. suggested the existence of solid oxides in samples below the threshold temperature [46], but DSC data in Figure 6.9 suggests that only a very small amount of oxides is possible. This could not cause such dramatic changes in viscosity.

Apparently, the viscosity hysteresis, the volume difference, and the overheating threshold temperature are mutually related to the same underlying cause: a phase transition. This could be a polymorphous liquid-to-liquid phase transition as mentioned by Busch *et al.*, or phase separation which was reported to occur at lower temperature about 680 K [47].

A polymorphous liquid-liquid phase transition should have a single transition temperature, but the volume differences in Figure 6.6 are temperature related. This suggests a continuous composition behavior.

The phase separation seems to be the plausible explanation for the experimental results. If this is true, then composition changes in the liquid should occur during the cooling. This might be the cause of an asymmetric eutectic zone behavior discussed by Li [48].

The DSC data on Vit1 is shown in Figure 6.12 for a graphite crucible and an alumina crucible. They show no evidence of crystal melting above liquidus temperature. The heat released for the graphite crucible at 970 ℃ may be caused by the chemical reaction of liquid Vit1 and graphite as already observed by Masuhr [49].

[#] Instrument	File	Identity	Sample	Date	Mass	Segment	Range	Atmosphere	Correction
[1] NETZSCH DSC 404C	LM1_0021_Rolex1mmTip...	1 mm rod, end of a.m. cast	LM1 tip from Rolex cast	4/16/2009 12:05:00 PM	36.300 mg	1/1	50.0/20.00(K/min)/1100.0	Ar/50 / ---/---	020
[2] NETZSCH DSC 404C	LM1_0021_Rolex1mmTip...	1 mm rod, end of a.m. cast	LM1 tip from Rolex cast	4/20/2009 3:36:03 PM	33.200 mg	1/1	30.0/20.00(K/min)/1100.0	Ar/50 / ---/---	020

Figure 6.12: DSC measurement on Vit1 in both graphite crucible and alumina crucible (darker)

6.6 References

[1] D. Turnbull And R. E. Cech, Journal Of Applied Physics **21**, 804 (1950).

[2] W. Klement, R. H. Willens, And P. Duwez, Nature **187**, 869 (1960).

[3] H. S. Chen And D. Turnbull, Acta Metallurgica **18**, 261 (1970).

[4] A. Inoue, T. Zhang, And T. Masumoto, Materials Transactions Jim **31**, 177 (1990).

[5] A. Peker And W. L. Johnson, Applied Physics Letter **63**, 2342 (1993).

[6] W. L. Johnson, MRS Bull. **24**, 42 (1999).

[7] M. F. De Oliveira, W. J. Botta, C. S. Kiminami, A. Inoue, And A. R. Yavari, Applied Physics Letter **81**, 1606 (2002).

[8] A. Wiest, G. Duan, M. D. Demetriou, L. A. Wiest, A. Peck, G. Kaltenboeck, B. Wiest, And W. L. Johnson, Acta Materialia **56**, 2625 (2008).

[9] A. Wiest, J. S. Harmon, M. D. Demetriou, R. D. Conner, And W. L. Johnson, Scripta Materialia **60**, 160 (2009).

[10] M. D. Demetriou, G. Duan, C. Veazey, K. De Blauwe, And W. L. Johnson, Scripta Materialia **57**, 9 (2007).

[11] M. D. Demetriou, C. Veazey, J. Schroers, J. C. Hanan, And W. L. Johnson, (Elsevier Science Sa, 2007), p. 92.

[12] J. Schroers, C. Veazey, M. D. Demetriou, And W. L. Johnson, Journal Of Applied Physics **96**, 7723 (2004).

[13] C. Veazey, M. D. Demetriou, J. Schroers, J. C. Hanan, L. A. Dunning, W. F. Kaukler, And W. L. Johnson, Journal Of Advanced Materials **40**, 7 (2008).

[14] J. A. Wert, C. Thornsen, R. D. Jensen, And M. Arentoft, J. Mater. Process. Technol. **209**, 1570 (2009).

[15] J. Schroers, Q. Pham, And A. Desai, Journal Of Microelectromechanical Systems **16**, 240 (2007).

[16] J. Schroers, Q. Pham, A. Peker, N. Paton, And R. V. Curtis, Scripta Materialia **57**, 341 (2007).

[17] D. C. Hofmann, J. Y. Suh, A. Wiest, M. L. Lind, M. D. Demetriou, And W. L. Johnson, Proceedings Of The National Academy Of Sciences Of The United States Of America **105**, 20136 (2008).

[18] D. C. Hofmann, J. Y. Suh, A. Wiest, G. Duan, M. L. Lind, M. D. Demetriou, And W. L. Johnson, Nature **451**, 1085 (2008).

[19] T. H. Kim, G. W. Lee, A. K. Gangopadhyay, R. W. Hyers, J. R. Rogers, A. I. Goldman, And K. F. Kelton, (Iop Publishing Ltd, 2007).

[20] S. Mukherjee, H. Kang, W. Johnson, And W. Rhim, Physical Review B **70** (2004).

[21] S. Mukherjee, J. Schroers, W. Johnson, And W. Rhim, Physical Review Letters **94** (2005).

[22] S. Mukherjee, J. Schroers, Z. Zhou, W. Johnson, And W. Rhim, Acta Materialia **52**, 3689 (2004).

[23] S. Mukherjee, Z. Zhou, W. Johnson, And W. Rhim, Journal Of Non-Crystalline Solids **337**, 21 (2004).

[24] S. Mukherjee, Z. Zhou, J. Schroers, W. Johnson, And W. Rhim, Applied Physics Letter **84**, 5010 (2004).

[25] J. Schroers And W. L. Johnson, Physical Review Letters **93** (2004).

[26] G. Duan, A. Wiest, M. Lind, J. Li, W. Rhim, And W. Johnson, Advanced Materials **19**, 4272 (2007).

[27] M. C. Weinberg, D. R. Uhlmann, And E. D. Zanotto, Journal Of The American Ceramic Society **72**, 2054 (1989).

[28] M. C. Weinberg, Thermochimica Acta **280**, 63 (1996).

[29] C. V. Thompson, A. L. Greer, And F. Spaepen, Acta Metallurgica **31**, 1883 (1983).

[30] L. E. Tanner And R. Ray, Acta Metallurgica **27**, 1727 (1979).

[31] E. S. Park, J. H. Na, And D. H. Kim, Applied Physics Letter **91** (2007).

[32] J. Schroers And W. L. Johnson, Physical Review Letters **93** (2004).

[33] V. N. Novikov And A. P. Sokolov, Nature **431**, 961 (2004).

[34] C. A. Angell, Journal Of Non-Crystalline Solids **73**, 1 (1985).

[35] A. S. Argon, Acta Metallurgica **27**, 47 (1979).

[36] W. L. Johnson, M. D. Demetriou, J. S. Harmon, M. L. Lind, And K. Samwer, MRS Bull. **32**, 644 (2007).

[37] J. S. Harmon, M. D. Demetriou, And W. L. Johnson, Applied Physics Letter **90** (2007).

[38] C. A. Angell, K. L. Ngai, G. B. Mckenna, P. F. Mcmillan, And S. W. Martin, Journal Of Applied Physics **88**, 3113 (2000).

[39] F. Spaepen, Acta Metallurgica **25**, 407 (1977).

[40] G. J. Fan, M. Freels, H. Choo, P. K. Liaw, J. J. Z. Li, W. K. Rhim, W. L. Johnson, P. Yu, And W. H. Wang, Applied Physics Letter **89** (2006).

[41] G. Fan, J. Li, W. Rhim, D. Qiao, H. Choo, P. Liaw, And W. Johnson, Applied Physics Letter **88** (2006).

[42] A. Masuhr, R. Busch, And W. L. Johnson, (Elsevier Science Bv, 1999), P. 566.

[43] Z. Long, G. Xie, H. Wei, X. Su, J. Peng, P. Zhang, And A. Inoue, Materials Science And Engineering: A **509**, 23 (2009).

[44] C. Way, P. Wadhwa, And R. Busch, Acta Materialia **55**, 2977 (2007).

[45] S. Mukherjee, Z. Zhou, J. Schroers, W. L. Johnson, And W. K. Rhim, Applied Physics Letter **84**, 5010 (2004).

[46] X. Lin, W. Johnson, And W. Rhim, Materials Transactions Jim **38**, 473 (1997).

[47] B. V. De Moortele, T. Epicier, J. M. Pelletier, And J. L. Soubeyroux, Journal Of Non-Crystalline Solids **345-346**, 169 (2004).

[48] Y. Li, Jom **57**, 60 (2005).

[49] A. Masuhr, Ph. D. Thesis, Caltech, 1999.